



# Four decades of Antarctic surface elevation changes from multi-mission satellite altimetry

Ludwig Schröder<sup>1,2</sup>, Martin Horwath<sup>1</sup>, Reinhard Dietrich<sup>1</sup>, Veit Helm<sup>2</sup>, Michiel R. van den Broeke<sup>3</sup>, and Stefan R. M. Ligtenberg<sup>3</sup>

<sup>1</sup>Technische Universität Dresden, Institut für Planetare Geodäsie, Dresden, Germany

<sup>2</sup>Alfred Wegener Institute, Helmholtz Centre for Polar and Marine Research, Bremerhaven, Germany

<sup>3</sup>Institute for Marine and Atmospheric Research Utrecht, Utrecht University, Utrecht, the Netherlands

**Correspondence:** Ludwig Schröder (ludwig.schroeder@tu-dresden.de)

Received: 6 March 2018 – Discussion started: 19 March 2018

Revised: 13 January 2019 – Accepted: 16 January 2019 – Published: 5 February 2019

**Abstract.** We developed a multi-mission satellite altimetry analysis over the Antarctic Ice Sheet which comprises Seasat, Geosat, ERS-1, ERS-2, Envisat, ICESat and CryoSat-2. After a consistent reprocessing and a stepwise calibration of the inter-mission offsets, we obtained monthly grids of multi-mission surface elevation change (SEC) with respect to the reference epoch 09/2010 (in the format of month/year) from 1978 to 2017. A validation with independent elevation changes from in situ and airborne observations as well as a comparison with a firn model proves that the different missions and observation modes have been successfully combined to a seamless multi-mission time series. For coastal East Antarctica, even Seasat and Geosat provide reliable information and, hence, allow for the analysis of four decades of elevation changes. The spatial and temporal resolution of our result allows for the identification of when and where significant changes in elevation occurred. These time series add detailed information to the evolution of surface elevation in such key regions as Pine Island Glacier, Totten Glacier, Dronning Maud Land or Lake Vostok. After applying a density mask, we calculated time series of mass changes and found that the Antarctic Ice Sheet north of 81.5° S was losing mass at an average rate of  $-85 \pm 16 \text{ Gt yr}^{-1}$  between 1992 and 2017, which accelerated to  $-137 \pm 25 \text{ Gt yr}^{-1}$  after 2010.

## 1 Introduction

Satellite altimetry is fundamental for detecting and understanding changes in the Antarctic Ice Sheet (AIS; Rémy and Parouty, 2009; Shepherd et al., 2018). Since 1992, altimeter missions have revealed dynamic thinning of several outlet glaciers of the West Antarctica Ice Sheet (WAIS) and have put narrow limits on elevation changes in most parts of East Antarctica. Rates of surface elevation change are not constant in time (Shepherd et al., 2012). Ice flow acceleration has caused dynamic thinning to accelerate (Mouginot et al., 2014; Hogg et al., 2017). Variations in surface mass balance (SMB) and firn compaction rate also cause interannual variations of surface elevation (Horwath et al., 2012; Shepherd et al., 2012; Lenaerts et al., 2013). Consequently, different rates of change have been reported from altimeter missions that cover different time intervals. For example, ERS-1 and ERS-2 data over the interval 1992–2003 revealed negative elevation rates in eastern Dronning Maud Land and Enderby Land (25–60° E) and positive rates in Princess Elizabeth Land (70–100° E) (Wingham et al., 2006b), while Envisat data over the interval 2003–2010 revealed the opposite pattern (Flament and Rémy, 2012). Two large snowfall events in 2009 and 2011 induced stepwise elevation changes in Dronning Maud Land (Lenaerts et al., 2013; Shepherd et al., 2012).

As a consequence, mean linear rates derived from a single mission have limited significance in characterizing the long-term evolution of the ice sheet (Wouters et al., 2013). Data from different altimeter missions need to be linked over a time span that is as long as possible in order to better distin-

guish and understand the long-term evolution and the natural variability of ice sheet volume and mass.

Missions with similar sensor characteristics have been combined, e.g., by Wingham et al. (2006b, ERS-1 and ERS-2) and Li and Davis (2008, ERS-2 and Envisat). Fricker and Padman (2012) use Seasat, ERS-1, ERS-2 and Envisat to determine elevation changes of Antarctic ice shelves. They apply constant biases, determined over open ocean, to cross-calibrate the missions. In contrast to ocean-based calibration, Zwally et al. (2005) found significant differences for the biases over ice sheets with a distinct spatial pattern (see also Frappart et al., 2016). Khvorostovsky (2012) showed that the correction of inter-mission offsets over an ice sheet is not trivial. Paolo et al. (2016) cross-calibrated ERS-1, ERS-2 and Envisat on each grid cell using overlapping epochs, and Adusumilli et al. (2018) extended these time series by including CryoSat-2 data. We use a very similar approach for conventional radar altimeter measurements with overlapping mission periods. Moreover, we also include measurements of the nonoverlapping missions Seasat and Geosat and measurements with different sensor characteristics, such as ICESat laser altimetry or CryoSat-2 interferometric synthetic aperture radar (SARIn) mode, making the combination of the observations even more challenging.

Here we present an approach for combining seven different satellite altimetry missions over the AIS. Using refined waveform retracking and slope correction of the radar altimetry (RA) data, we ensure the consistency of the surface elevation measurements and improve their precision by up to 50 %. In the following stepwise procedure, we first process the measurements from all missions jointly using the repeat-altimetry method. We then form monthly time series for each individual mission data set. Finally, we merge all time series from both radar and laser altimetry. For this last step, we employ different approaches of inter-mission offset estimation, depending on the temporal overlap or nonoverlap of the missions and on the similarity or dissimilarity of their altimeter sensors.

We arrive at consistent and seamless time series of gridded surface elevation differences with respect to a reference epoch (09/2010; in the format of month/year) which we made publicly available at <https://doi.pangaea.de/10.1594/PANGAEA.897390> (Schröder et al., 2019). The resulting monthly grids with a 10 km spatial resolution were obtained by smoothing with a moving window over 3 months and a spatial Gaussian weighting with  $2\sigma = 20$  km. We evaluate our results and their estimated uncertainties by a comparison with independent in situ and airborne data sets, satellite gravimetry estimates and regional climate model outputs. We illustrate that these time series of surface elevation change (SEC) allow for the study of geometry changes and derived mass changes of the AIS in unprecedented detail. The recent elevation changes of Pine Island Glacier in West Antarctica, Totten Glacier in East Antarctica and Shirase Glacier of Dronning Maud Land in East Antarctica are put in context

with the extended time series from satellite altimetry. Finally, we calculate ice sheet mass balances from these data for the covered regions. A comparison with independent data indicates a high consistency of the different data sets but also reveals remaining discrepancies.

## 2 Data

### 2.1 Altimetry data

We use the ice sheet surface elevation observations from seven satellite altimetry missions: Seasat, Geosat, ERS-1, ERS-2, Envisat, ICESat and CryoSat-2. Figure 1 gives an overview of their temporal and spatial coverage. The data of the two early missions, Seasat and Geosat, were obtained from the Radar Ice Altimetry project at Goddard Space Flight Center (GSFC). For the ESA missions, we used the data of the REAPER reprocessing project (Brockley et al., 2017) of ERS-1 and ERS-2, the RA-2 Sensor and Geophysical Data Record (SGDR) of Envisat in version 2.1 and Baseline C Level 2I data of CryoSat-2. For ICESat we used GLA12 of release 633 from the National Snow and Ice Data Center (NSIDC). Further details concerning the data set versions used and the data-editing criteria applied to remove corrupted measurements in a preprocessing step are given in the Supplement.

As illustrated in Fig. 1, due to the inclination of 108°, Seasat and Geosat measurements only cover the coastal regions of the East Antarctic Ice Sheet (EAIS) and the northern tip of the Antarctic Peninsula Ice Sheet (APIS) north of 72° S, which is about 25 % of the total ice sheet area. With the launch of ERS-1, the polar gap was reduced to areas south of 81.5° S, resulting in coverage of 79 % of the area. The polar gap is even smaller for ICESat (86° S) and CryoSat-2 (88° S), leading to a nearly complete coverage of the AIS in recent epochs.

ERS-1 and ERS-2 measurements were performed in two different modes, distinguished by the width of the tracking time window and the corresponding temporal resolution of the recorded waveform. The ice mode is coarser than the ocean mode, in order to increase the chance of capturing the radar return from rough topographic surfaces (Scott et al., 1994). While the ice mode was employed for the majority of measurements, a significant number of observations have also been performed in the ocean mode over Antarctica (22 % for ERS-1, 2 % for ERS-2). We use the data from both modes, as the ocean mode provides a higher precision while the ice mode is more reliable in steep terrain (see Figs. S1 and S3 in the Supplement). However, as there is a regionally varying bias between the modes, we treat them as two separate data sets, similar to Paolo et al. (2016).

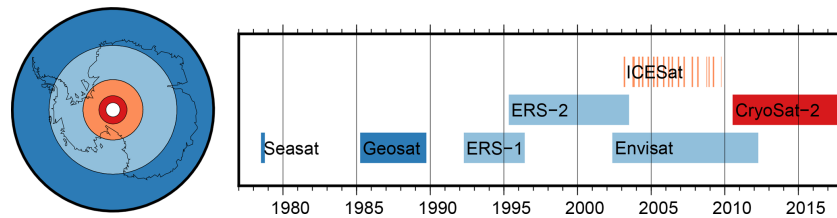


**Figure 1.** Spatial and temporal coverage of the satellite altimetry data used in this study. The colors denote the maximum southern extent of the measurements (dark blue: 72° S, light blue: 81.5° S, orange: 86° S, red: 88° S) and thus the size of the respective polar gap.

## 2.2 Reprocessing of radar altimetry

Compared to measurements over the global oceans, pulse-limited radar altimetry (PLRA) over ice sheets requires a specific processing to account for the effects of topography and the dielectric properties of the surface (Bamber, 1994). To ensure consistency in the analysis of PLRA measurements, processed and provided by different institutions, we applied our own method for retracking and slope correction.

The slope correction is applied to account for the effect of topography within the beam-limited footprint (Brenner et al., 1983). Different approaches exist to apply a correction (Bamber, 1994), but this effect is still a main source of error in RA over ice sheets. The “direct method” uses the surface slope within the beam-limited footprint to obtain a correction for the measurement in the nadir direction. In contrast, the “relocation method” relates the measurement towards the likely true position up slope. While the direct method has the advantage that the measurement location is unchanged, which allows an easier calculation of profile crossovers or repeat-track parameters, the relocation method has lower intrinsic error (Bamber, 1994). A validation using crossovers with kinematic GNSS-profiles (Schröder et al., 2017) showed that, especially in coastal regions, the direct method leads to significantly larger offsets and standard deviations, compared to the relocation method. Roemer et al. (2007) developed a refined version of the relocation method, using the full information of a digital elevation model (DEM) to locate the point of closest approach (POCA) within the approximately 20 km beam-limited footprint. We applied this method in our reprocessing chain using the DEM of Helm et al. (2014). The CryoSat-2 measurements, used for this DEM, have very dense coverage, and hence very little interpolation is necessary. Compared to the DEM of Bamber et al. (2009), this significantly improves the spatial consistency. We optimized the approach of Roemer et al. (2007) with respect to computational efficiency for application over the entire ice sheet. Instead of searching the POCA with the help of a moving window of 2 km (which represents the pulse-limited footprint) in the DEM-to-satellite grid, we applied a Gaussian filter with  $\sigma = 1$  km to the DEM itself to resemble the coverage of a pulse-limited footprint. Hence, instead of the closest window average, we can simply search for the closest cell in the smoothed grid, which we use as the coarse POCA loca-

tion. In order to achieve a subgrid POCA location, we fit a bi-quadratic function to the satellite-to-surface distance within a  $3 \times 3$  grid cell environment around the coarse POCA grid cell and determine the POCA according to this function.

The retracking of the return signal waveform is another important component in the processing of RA data over ice sheets (Bamber, 1994). Functional fit approaches (e.g., Martin et al., 1983; Davis, 1992; Legrésy et al., 2005; Wingham et al., 2006b) are well established and allow the interpretation of the obtained waveform shape parameters with respect to surface and subsurface characteristics (e.g., Lacroix et al., 2008; Nilsson et al., 2015). However, the alternative approach of threshold retrackers has proven to be more precise in terms of repeatability (Davis, 1997; Nilsson et al., 2016; Schröder et al., 2017). A very robust variant is called ICE-1, using the “offset center of gravity” (OCOG) amplitude (Wingham et al., 1986). Compared to the waveform maximum, the OCOG amplitude is significantly less affected by noise (Bamber, 1994). Davis (1997) compared different retrackers and showed that a threshold-based retracker produces remarkably higher-precision results (especially with a low threshold as 10 %), compared to functional-fit-based results. We implemented three threshold levels (10 %, 20 % and 50 %) for the OCOG amplitude, which allowed us to analyze the influence of the choice of this level, similar to Davis (1997).

In addition to PLRA, we also use the SARIn mode data of CryoSat-2, reprocessed by Helm et al. (2014). The difference with respect to the processing by ESA mainly consisted of a refined determination of the interferometric phase and of the application of a threshold retracker.

## 2.3 Accuracy and precision

The accuracy of RA-derived ice surface elevation measurements has been assessed previously by a crossover comparison with independent validation data such as the ICESat laser observations (Brenner et al., 2007), airborne lidar (Nilsson et al., 2016) and ground-based GNSS profiles (Schröder et al., 2017). Besides the offset due to snowpack penetration and instrumental calibration over flat terrain, these assessments revealed that, with increasingly rough surface topography, the RA measurements show systematically higher elevations than the validation data. These topography-related

offsets can be explained by the fact that for surfaces that undulate within the  $\sim 20$  km beam-limited footprint, the radar measurements tend to refer to local topographic maxima (the POCA), while the validation data from ground-based GNSS profiles or ICESat-based profiles represent the full topography. The standard deviation of differences between RA data and validation data contains information about the measurement noise but is additionally influenced by the significantly different sampling of a rough surface as well. While over flat terrain, this standard deviation is below 50 cm for most satellite altimeter data sets, it can reach 10 m and more in coastal regions. However, both types of error relate to the different sampling of topography of the respective observation techniques. An elevation change, detected from within the same technique, is not influenced by these effects. Hence, with respect to elevation changes, not the accuracy but the precision (i.e., the repeatability) has to be considered.

This precision can be studied using intra-mission crossovers between ascending and descending profiles. Here, the precision of a single measurement is obtained by  $\sigma_H = |\Delta H|/\sqrt{2}$  as two profiles contribute to this difference. To reduce the influence of significant real surface elevation changes between the two passes, we only consider crossovers with a time difference of less than 31 days. In stronger inclined topography, the precision of the slope correction dominates the measurement error (Bamber, 1994). Hence, to provide meaningful results, the surface slope needs to be taken into consideration. We calculate the slope from the CryoSat-2 DEM (Helm et al., 2014). The absence of slope-related effects on flat terrain allows for the study of the influence of the retracker (denoted as noise here). With increasing slope, the additional error due to topographic effects can be identified.

A comparison of the crossover errors of our reprocessed data and of the standard products shows significant improvements achieved by our reprocessing. Figure 2 shows this comparison for Envisat (similar plots for each data set can be found in Fig. S1), binned into groups of  $0.05^\circ$  of specific surface slope. The results for a flat topography show that a 10 % threshold provides the highest precision, which confirms the findings of Davis (1997). For higher slopes, we see that our refined slope correction also contributed to a major improvement. A constant noise level  $\sigma_{\text{noise}}$  and a quadratic, slope-related term  $\sigma_{\text{slope}}$  have been fitted to the data according to  $\sigma_H = \sigma_{\text{noise}} + \sigma_{\text{slope}} \cdot s^2$ , where  $s$  is in the unit of degrees. The results in Table 1 show that for each of the PLRA data sets of ERS-1, ERS-2 and Envisat, the measurement noise could be reduced by more than 50 % compared to the ESA product which uses the functional fit retracker ICE-2 (Legréy and Rémy, 1997). With respect to the CryoSat-2 standard retracker (Wingham et al., 2006a), the improvement is even larger. Improvements are also significant for the slope-related component. For the example of Envisat and a slope of  $1^\circ$ , the slope-related component is 1.03 m for the ESA product and only 0.37 m for the reprocessed data. The advanced interferometric processing of the SARIn data achieved similar im-

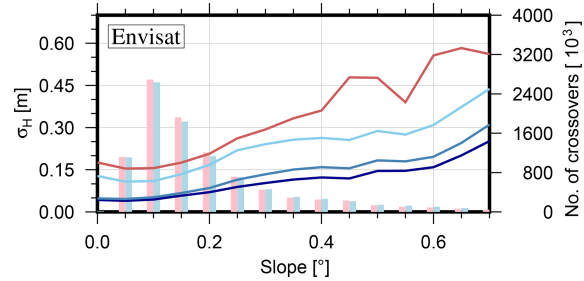


**Figure 2.** Precision of different processing versions of Envisat measurements from near-time ( $< 31$  days) crossovers, binned against slope. Red curve: ESA version with ICE-2 retracker and relocated by mean surface slope. Light, medium and dark blue curves: data reprocessed in this study with 50 %-, 20 %- and 10 %-threshold retracker, relocated using the refined method. Vertical bars: number of crossovers for the ESA (red) and our 10 % threshold retracked data (blue).

**Table 1.** Noise level and slope-related component ( $s$  in degrees) of the measurement precision, fitted to near-time crossovers (unit: m) of the data from the respective data center and our reprocessed data (with a 10 % threshold retracker applied).

Data set	Data center	Reprocessed
Seasat	$0.21 + 1.91s^2$	$0.25 + 0.70s^2$
Geosat	$0.17 + 0.86s^2$	$0.18 + 1.16s^2$
ERS-1 (ocean)	$0.25 + 0.90s^2$	$0.09 + 0.18s^2$
ERS-1 (ice)	$0.36 + 2.37s^2$	$0.17 + 0.57s^2$
ERS-2 (ocean)	$0.23 + 0.75s^2$	$0.07 + 0.14s^2$
ERS-2 (ice)	$0.38 + 2.57s^2$	$0.15 + 0.53s^2$
Envisat	$0.17 + 1.03s^2$	$0.05 + 0.37s^2$
ICESat	$0.05 + 0.25s^2$	
CryoSat-2 (LRM)	$0.18 + 2.46s^2$	$0.03 + 1.06s^2$
CryoSat-2 (SARIn)	$0.38 + 2.01s^2$	$0.11 + 0.79s^2$

Note that the slope-dependent component is weakly determined for data sets with poor tracking in rugged terrain such as Seasat, Geosat or the ERS ocean mode and for the LRM mode of CryoSat-2.

provements. For the two early missions Seasat and Geosat, the crossover error of our reprocessed profiles is similar to that of the original data set from GSFC. However, the number of crossover points is significantly increased, especially for Geosat (see Fig. S1). This means that our reprocessing obtained reliable data where the GSFC processor rejected the measurements.

In addition to measurement noise, reflected in the crossover differences, a consistent pattern of offsets between ascending and descending tracks has been observed previously (A–D bias; Legréy et al., 1999; Arthern et al., 2001). Legréy et al. (1999) interpret this pattern as an effect of the interaction of the linearly polarized radar signal with wind-induced surface structures, while Arthern et al. (2001) attribute the differences to anisotropy within the snowpack. Helm et al. (2014) showed that a low threshold retracker sig-

nificantly reduces the A–D bias. We observe a similar major reduction (from  $\pm 1$  m in some regions for a functional fit retracker to  $\pm 15$  cm when using a 10 % threshold; see Fig. S2). The remaining bias is not larger, in its order of magnitude, than the respective noise. Moreover, near the ice sheet margins, the determination of meaningful A–D biases is complicated by the broad statistical distribution of A–D differences and the difficulty of discriminating outliers. We therefore do not apply a systematic A–D bias as a correction but rather include its effect in the uncertainty estimate of our final result.

### 3 Multi-mission SEC time series

#### 3.1 Repeat-track parameter fit

We obtain elevation time series following the repeat-track approach, similar to Legrésy et al. (2006) and Flament and Rémy (2012). As the orbits of the missions used here have different repeat-track patterns, instead of along-track boxes we perform our fit on a regular grid with 1 km spacing (as in Helm et al., 2014). For each grid cell we analyze all elevation measurements  $h_i$  within a radius of 1 km around the grid cell center. This size seems reasonable as for a usual along-track spacing of about 350 m for PLRA (Rémy and Parouty, 2009), each track will have up to five measurements within the radius. Due to the size of the pulse-limited footprint, a smaller search radius would contain only PLRA measurements with very redundant topographic information and thus would not be suitable to fit a reliable correction for the topography. As specified in Eq. (1), the parameters contain a linear trend ( $dh/dt$ ), a planar topography ( $a_0, a_1, a_2$ ) and a regression coefficient (dBS) for the anomaly of backscattered power ( $bs_i - \bar{bs}$ ) to account for variations in the penetration depth of the radar signal.

For a single mission, the parameters are adjusted according to the following model:

$$\begin{aligned} h_i = & dh/dt(t_i - t_0) + \\ & a_0 + a_1 x_i + a_2 y_i + \\ & \text{dBS} (bs_i - \bar{bs}) + \\ & \text{res}_i. \end{aligned} \quad (1)$$

Here,  $t_i$  denotes the time of the observation. The reference epoch  $t_0$  is set to 09/2010.  $x_i$  and  $y_i$  are the polar stereographic coordinates of the measurement location, reduced by the coordinates of the cell's center. The residual  $\text{res}_i$  describes the misfit between the observation and the estimated parameters.

To account for varying penetration depths due to variations in the electromagnetic properties of the ice sheet surface, different approaches exist. Wingham et al. (1998), Davis and Ferguson (2004), McMillan et al. (2014) and Zwally et al. (2015) apply a linear regression using the backscattered power. Flament and Rémy (2012), Michel et al. (2014)

and Simonsen and Sørensen (2017) use two additional waveform shape parameters, obtained from functional fit retrackers. Nilsson et al. (2016) showed that a low threshold retracker mitigates the need for a complex waveform shape correction. Hence, we decided to use a solely backscatter-related correction.

Besides the parameters in Eq. (1), McMillan et al. (2014) and Simonsen and Sørensen (2017) estimate an additional orbit-direction-related parameter to account for A–D biases. In Sect. 2.3 we showed that these biases are significantly reduced due to reprocessing with a low threshold retracker. A further reduction of possible remaining artifacts of A–D biases is achieved by smoothing in the merging step in Sect. 3.3.3. The weighted averaging of the results over a diameter of 60 km leads to a balanced ratio of ascending and descending tracks. Our choices concerning the correction for local topography, time-variable penetration effects and A–D biases were guided by the principle of preferring the simplest viable model in order to keep the number of parameters small compared to the number of observations.

In contrast to this single mission approach, here we perform a combined processing of all data from different missions and even different altimeter techniques. Thus, some of the parameters may vary between the data sets. To allow for offsets between the missions, the elevation at the cell center  $a_0$  is fitted for each mission individually. The same applies to dBS, which might relate to specific characteristics of a mission as well. For Seasat, covering less than 100 days, this parameter is not estimated, as we assume that during the mission lifetime no significant changes occurred. For ICE-Sat, dBS is not estimated either, as signal penetration is negligible for the laser measurements.

Between different observation techniques (i.e., PLRA, SARIn and laser altimetry), the effective surface slope may also differ. Considering the specific footprint sizes and shapes, the topography is sampled in a completely different way as illustrated in Fig. 3. While PLRA refers to the closest location anywhere within the  $\sim 20$  km beam-limited footprint (i.e., the POCA), CryoSat's SARIn measurement can be attributed within the narrow Doppler stripe in the cross-track direction. For ICESat the  $\sim 70$  m laser spot allows a much better sampling of local depressions. Hence, the slope parameters  $a_1$  and  $a_2$  are estimated for each of the techniques independently.

Considering these sensor-specific differences, the model for the least squares adjustment in Eq. (1) is extended for multi-mission processing to

$$\begin{aligned} h_i = & dh/dt(t_i - t_0) + \\ & a_{0,M(i)} + a_{1,T(i)} x_i + a_{2,T(i)} y_i + \\ & \text{dBS}_{M(i)} (bs_i - \bar{bs}_{M(i)}) + \\ & \text{res}_i, \end{aligned} \quad (2)$$

where  $M(i)$  and  $T(i)$  denote to which mission or technique the measurement  $h_i$  belongs.

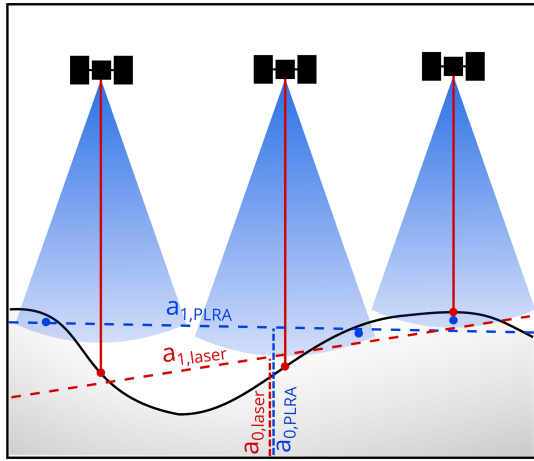


**Figure 3.** Illustration of the technique-dependent topographic sampling. The laser (red) measures the surface elevation in the nadir of the instrument, while for radar altimetry (blue) the first return signal originates from the POCA (marked by the blue point). Hence, planar surface approximations to the measured heights (dashed lines) as in Eq. (2) are intrinsically different for the different techniques.

We define a priori weights for the measurements  $h_i$  based on the precision of the respective mission and mode from crossover analysis (Table 1) and depending on the surface slope at the measurement location. This means that in regions with a more distinctive topography, ICESat measurements (with a comparatively low slope-dependent error component) will obtain stronger weights, compared to PLRA as Envisat. Over regions of flat topography, such as the interior of East Antarctica, the weights between PLRA and ICESat are comparable.

In order to remove outliers from the data and the results we apply different outlier filters. After the multi-mission fit, we screen the standardized residuals (Baarda, 1968) to exclude any  $\text{res}_i$  that exceed 5 times its a posteriori uncertainty. We iteratively repeat the parameter fit until no more outliers are found. Furthermore, in order to exclude remaining unrealistic results from further processing, we filter our repeat-track cells and reject any results where we obtain an absolute elevation change rate  $|\text{dh}/\text{dt}|$  which is larger than  $20 \text{ m yr}^{-1}$  or where the standard deviation of this rate is higher than  $0.5 \text{ m yr}^{-1}$ .

### 3.2 Single-mission time series

After fitting all parameters according to the multi-mission model (Eq. 2), we regain elevation time series by recombining the parameters  $a_0$  and  $\text{dh}/\text{dt}$  with monthly averages of the residuals ( $\text{res}$ ). For each month  $j$  and each mission  $M$ , the time series are constructed as

$$h_{j,M} = a_{0,M} + \text{dh}/\text{dt}(t_j - t_0) + \overline{\text{res}}_{j,M}. \quad (3)$$

This recombination of parameters from Eq. (2) and averages of residuals does not include the parameters of topography slope and backscatter regression. Hence, each time series of  $h_{j,M}$  relates to the cell center and is corrected for time-variable penetration effects. Due to the reference elevation  $a_{0,M}$ , which may also contain the inter-mission offset, the penetration depth and a component of the topography sampling within the cell, this results in individual time series for each single mission. A schematic illustration of the results of this step is given in Fig. 5a. The temporal resolution of these time series is defined by using monthly averages of the residuals. With typical repeat-cycle periods of 35 days or more, these  $\bar{\text{res}}$  typically represent the anomalies of a single satellite pass towards all parameters including the linear rate of elevation change. The standard deviation of the residuals in these monthly averages is used as uncertainty measure for  $h_{j,M}$  (see Sect. S3.1 for further details).

### 3.3 Combination of the single-mission time series

In order to merge data from different missions into a joint time series, inter-mission offsets have to be determined and eliminated. In the ERS reprocessing project (Brockley et al., 2017), mean offsets between the ERS missions and Envisat have been determined and applied to the elevation data. However, for ice sheet studies inter-satellite offsets are found to be regionally varying (Zwally et al., 2005; Thomas et al., 2008; Khvorostovsky, 2012). When merging data from different observation techniques (PLRA, SARIn and laser) the calibration gets even more challenging. We chose an approach in different steps which is depicted in Figs. 4 and 5. The following section gives an overview and explains the different steps to merge the single mission time series. A detailed description of the parameters used in each step can be found in the Supplement.

#### 3.3.1 Merging PLRA time series

In the first step, we merge the PLRA time series. For these missions the topographic sampling by the instruments is similar and thus the offsets are valid over larger regions. For overlapping missions (ERS-1, ERS-2, Envisat, CryoSat-2 LRM) the offsets are calculated from simultaneous epochs (blue area in Fig. 5b), as performed by Wingham et al. (1998) or Paolo et al. (2016). Smoothed grids of these offsets are generated, summed up if necessary to make all data sets comparable with Envisat (see Fig. S4) and applied to the respective missions. For the ERS missions, we find significant differences in the offsets for ice and ocean mode; hence, we determine separate offsets for each mode. Comparing our maps with similar maps of offsets between ERS-2 (ice mode) and Envisat shown by Frappart et al. (2016) reveals that the spatial pattern agrees very well, but we find significantly smaller amplitudes. We interpret this as a reduced influence of volume scattering due to our low retracking threshold. In ac-

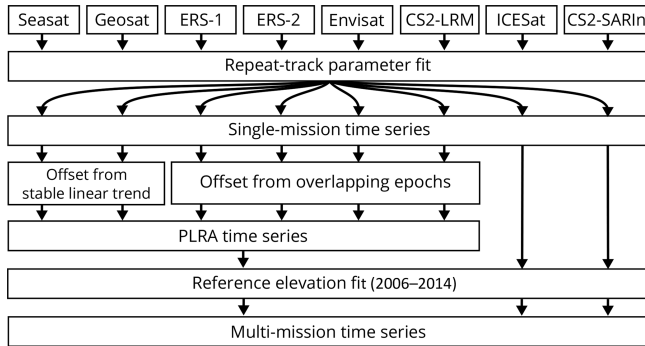


**Figure 4.** Schematic diagram of the processing steps from the combined repeat-track parameter fit over single-mission time series towards a combined multi-mission time series.

cordance with Zwally et al. (2005), we did not find an appropriate functional relationship between the offset and the waveform parameters.

To calibrate Geosat and Seasat, a gap of several years without observations has to be bridged. As depicted by the dashed blue lines in Fig. 5b, we do this using the trend-corrected reference elevations  $a_{0,M}$  from the joint fit in Eq. (2). This, however, can only be done if the rate is sufficiently stable over the whole period. Therefore, we use two criteria. First, we check the standard deviation of the fit of  $dh/dt$ . This  $\sigma_{dh/dt}$  indicates the consistency of the observations towards a linear rate during the observational period. However, anomalies during the temporal gaps between the missions (i.e., 1978–1985 and 1989–1992) cannot be detected in this way. Therefore, we further utilize a firn densification model (FDM; Ligtenberg et al., 2011; van Wessem et al., 2018). This model describes the anomalies in elevation due to atmospheric processes against the long-term mean. The root mean square (rms) of the FDM time series is hence a good measure for the magnitude of the nonlinear variations in surface elevation. Consequently, only cells where  $\sigma_{dh/dt} < 1 \text{ cm yr}^{-1}$  and  $\text{rms}_{\text{FDM}} < 20 \text{ cm}$ , indicating a highly linear rate, are used to calibrate the two historic missions. Maps of the offsets with respect to Envisat are shown in Fig. S5. The FDM criterion is not able to detect changes in ice dynamics. However, as regions where both stability criteria are fulfilled are mainly found on the plateau where flow velocity is below  $30 \text{ m yr}^{-1}$  (Rignot et al., 2017), we expect no significant nonlinear elevation changes due to ice flow. The mean of the offsets over all cells amounts to  $-0.86 \text{ m}$  for Seasat and  $-0.73 \text{ m}$  for Geosat. The corresponding standard deviations of  $0.85$  and  $0.61 \text{ m}$  are mainly a result of the regional pattern of the offsets. The true offsets are likely to have spatial variations. However, we are not able to distinguish spatial variations of the offset from residual effects of temporal height variations in the regions meeting the stability criterion. In the regions not meeting this criterion, we are not able to estimate the spatial variations of the offset at all. Therefore,

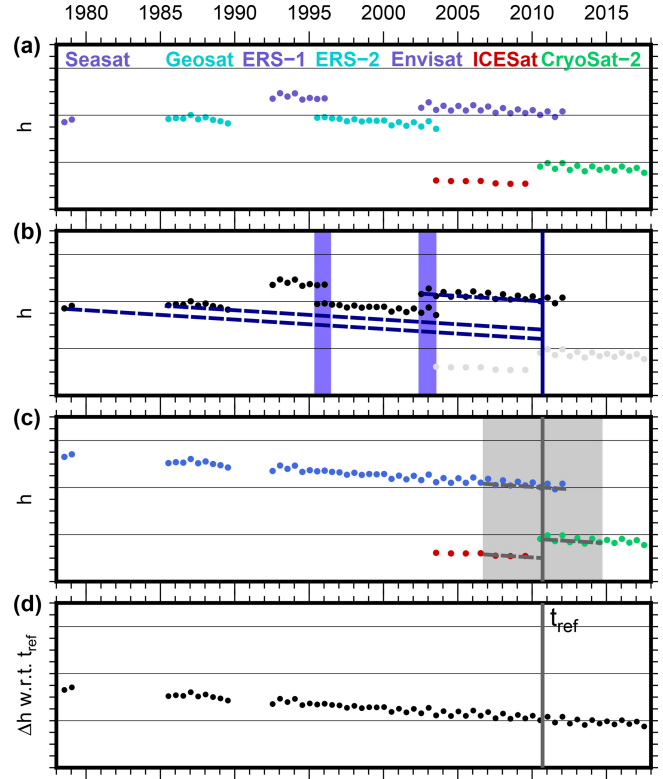


**Figure 5.** Schematic illustration of the combination of the missions. **(a)** Single-mission time series of PLRA missions (blue and cyan), CryoSat-2 in SARIn mode (green) and the laser altimetry measurements of ICESat (red) with inter-mission offsets. **(b)** Offsets between the PLRA data are determined from overlapping epochs (blue area) or trend-corrected elevation differences (according to Eq. 2) where  $dh/dt$  is sufficiently stable. **(c)** The specific offset between PLRA, SARIn and laser data depends on the sampling of the topography within each single cell. These different techniques are aligned by reducing each elevation time series by the specific elevation at the reference epoch  $t_{\text{ref}}$ . Due to possible nonlinear surface elevation changes, this reference elevation is obtained from an 8-year interval only (gray area). **(d)** The combined multi-mission time series contains SECs with respect to  $t_{\text{ref}}$ .

our final estimate of the offset, applied to the measurements, is a constant, calculated as the average offset over the regions meeting the stability criterion. The spatial variability not accounted for by the applied offset is included, instead, in the assessed uncertainty. Our bias between Seasat and Envisat ( $-0.86 \pm 0.85 \text{ m}$ ) agrees within uncertainties with the ocean-based bias of  $-0.77 \text{ m}$  used by Fricker and Padman (2012). However, we prefer the offset determined over the ice sheet because this kind of offset may depend on the reflecting medium (see Sect. S3.2.2 for a more detailed discussion).

With the help of these offsets, all PLRA missions were corrected towards the chosen reference mission Envisat. Uncertainty estimates of the offsets are applied to the respective time series to account for the additional uncertainty. Hence,

the PLRA time series are combined (blue in Fig. 5c with additional CryoSat-2 LRM mode where available). At epochs when more than one data set exists, we apply weighted averaging using the uncertainty estimates.

### 3.3.2 Technique-specific surface elevation changes

In contrast to the PLRA data in the previous step, when merging data from different observation techniques such as CryoSat's SARIn mode, ICESat's laser observations and PLRA, the different sampling of topography also has to be considered. As noted in Sect. 3.1, this might lead to completely different surfaces fitted to each type of elevation measurement and the time series need to be calibrated for each cell individually. However, not all cells have valid observations of each data set. Therefore, instead of calibrating the techniques against each other, we reduce each time series by their elevation at a common reference epoch and hence obtain time series of surface elevation changes (SEC) with respect to this reference epoch instead of absolute elevation time series. This step eliminates offsets due to differences in firm penetration or due to the system calibration between the techniques as well.

We chose September 2010 (09/2010) as the reference epoch. This epoch is covered by the observational periods of PLRA and CryoSat SARIn and also is exactly 1 year after the last observations of ICESat, which reduces the influence of an annual cycle. As discussed in Sect. 3.3.1, nonlinear elevation changes will adulterate  $a_0$  from Eq. (2), obtained over the full time span. Therefore, we applied another linear fit to a limited time interval of 8 years only (September 2006–September 2014, gray area in Fig. 5c). We subtract the variation of the FDM over this period to account for short-term variations. The limited time interval reduces the influence of changes in ice dynamics. We estimate the individual reference elevations  $a_{0,T}$  for each technique  $T$  and a joint  $dh/dt$ . After subtracting the technique-specific reference elevations  $a_{0,T}$  from the respective time series, they all refer to 09/2010 and can be combined.

### 3.3.3 Merging different techniques

We perform the final combination of the techniques using a weighted spatiotemporal averaging with  $10\text{ km}$   $\sigma$  Gaussian weights in the spatial domain (up to a radius of  $3\sigma = 30\text{ km}$ ) and over 3 epochs (i.e., including the two consecutive epochs) in the temporal domain. Hence, we obtain grids of surface elevation change (SEC) with respect to 09/2010 for each month observed. Due to the smoothing of the weighting function, we reduce our spatial SEC grid resolution to  $10\text{ km} \times 10\text{ km}$ . The respective uncertainties are calculated according to the error propagation. To avoid extrapolation and to limit this merging step to the observed area only, we calculate a value for an epoch in the  $10\text{ km} \times 10\text{ km}$  grid cells only if we have data within  $20\text{ km}$  around the cell center

(which is about the size of a beam-limited radar footprint). The five examples in Fig. 6 demonstrate the spatiotemporal coverage of the resulting SEC grids at different epochs. The corresponding uncertainty estimates, given in Fig. 6b (further details in the Supplement), reach values of  $1\text{ m}$  and more. Besides the measurement noise and the uncertainties of the offsets, these uncertainty estimates contain a further component from the weighted averaging. In regions with large variations in  $\Delta h$  over relatively short spatial scales (such as at fast-flowing outlet glaciers), such variations can add a significant contribution to  $\sigma_{\Delta h}$ . As the magnitude of  $\Delta h$  grows with the temporal distance to the reference epoch, the largest contributions to  $\sigma_{\Delta h}$  can be expected for the earliest epochs. This also explains why the epoch 09/2008 provides the lowest uncertainty estimate in these examples, even lower than the CryoSat-2-based epoch 09/2017.

## 4 Comparison of SEC with independent data

### 4.1 In situ and airborne observations

To validate our results, we used inter-profile crossover differences of 19 kinematic GNSS profiles (available for download from Schröder et al., 2016) and elevation differences from Operation IceBridge (OIB ATM L4; Studinger, 2014). The ground-based GNSS profiles were observed between 2001 and 2015 on traverse vehicles of the Russian Antarctic Expedition and most of them covered more than  $1000\text{ km}$ . The accuracy of these profiles has been determined in Schröder et al. (2017) to  $4\text{--}9\text{ cm}$ . One profile (K08C) has not been used due to poorly determined antenna height offsets. For each crossover difference between kinematic profiles from different years, we compare the differences of the corresponding altimetric SEC epochs in this location ( $\delta\Delta h = \Delta h_{\text{KIN}} - \Delta h_{\text{ALT}}$ ). The same analysis has been performed with the elevation changes obtained from differences of measurements of the scanning laser altimeter (Airborne Topographic Mapper, ATM) of OIB. As described by Studinger (2014), the Level 4  $\Delta h$  product is obtained by comparing planes fitted to the laser scanner point clouds. The flights, carried out between 2002 and 2016, were strongly concentrated along the outlet glaciers of West Antarctica and the Antarctic Peninsula. Hence, they cover much more rugged terrain, which is more challenging for satellite altimetry. Over the tributaries of the Amundsen Sea glaciers and along the polar gap of ICESat, some repeated measurements have also been performed over flat terrain. The accuracy of these airborne measurements has been validated, e.g., near summit station in Greenland. Brunt et al. (2017) used ground-based GNSS profiles of snowmobiles for this task and obtained offsets on the order of only a few centimeters and standard deviations between 4 and  $9\text{ cm}$ .

Figure 7a and d show the results of our validation (more detailed maps for several regions at Fig. S6). A satellite cal-

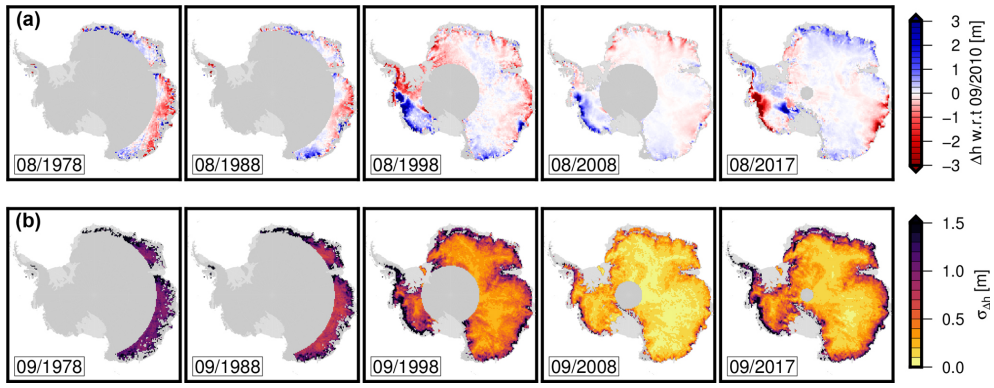


**Figure 6.** Five example snapshots of the resulting combined surface elevation time series (a) and their corresponding uncertainty (b). The height differences refer to our reference epoch 09/2010.

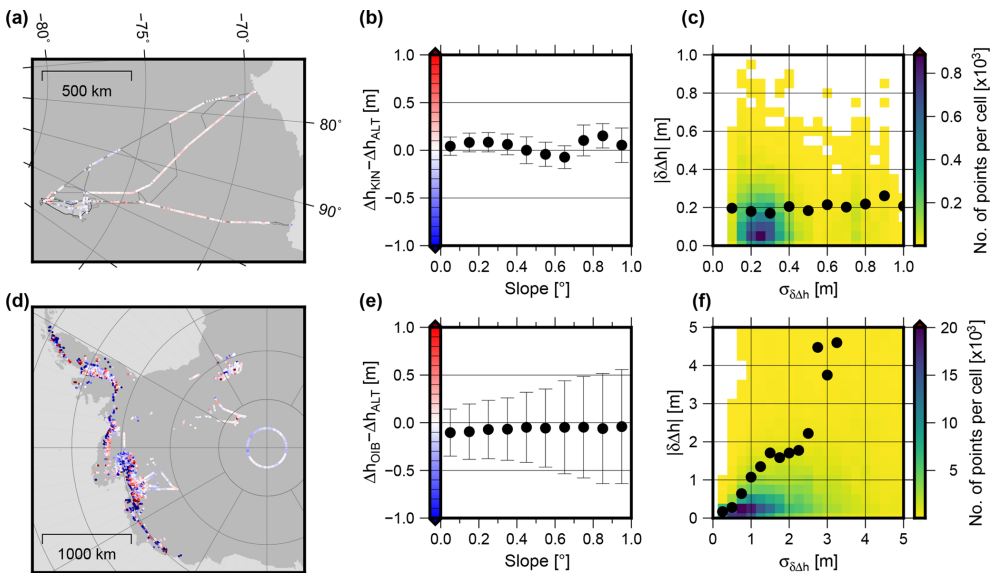


**Figure 7.** Validation with elevation differences observed by kinematic GNSS between 2001 and 2015 (a, b, c) and Operation IceBridge between 2002 and 2016 (d, e, f). Differences between elevation changes observed by the validation data and altimetry are shown in the maps (a, d, color scale in panels b and e). Median and MAD of these differences, binned by different surface slope, are shown in the center (b, e). The right diagrams (c, f) show the comparison of these differences with the respective uncertainty estimate, obtained from both data sets. The point density is plotted from yellow to blue and the black dots show the root mean square, binned against the estimated uncertainty.

ibration error would lead to systematic biases between the observed elevation differences if  $\Delta h_{ALT}$  is obtained from data of two different missions. However, such biases may also be caused by systematic errors in the validation data. Furthermore, in contrast to the calibration data, the RA measurements may systematically miss some of the most rapid changes if those are located in local depressions (Thomas et al., 2008). With an overall median difference of  $6 \pm 10$  cm for the GNSS profiles and  $-9 \pm 42$  cm for OIB, however, the observed elevation changes show only moderate systematic effects and agree within their error bars. The median absolute deviation (MAD) for different specific surface slopes (Fig. 7b and e) reveals the influence of topography in this validation. The GNSS profiles show only a very small increase of this

variation with slope. The IceBridge data cover the margins of many West Antarctic glaciers, where elevation changes differ over relatively short distances. Hence, it is not surprising that we see a significantly larger spread of  $\delta\Delta h$  at higher slopes here. However, in the less inclined regions, the MAD of the differences is still at a level of 25 cm, which is significantly larger than in the comparison with the GNSS profiles. This large spread for regions with low slopes originates mainly from the tributaries of Pine Island Glacier, where many campaigns of OIB are focused (see Figs. 7d and S6d for details). While still relatively flat, the surface elevation in this area is comparatively low, which leads to a stronger influence of precipitation (Fyke et al., 2017). This induces higher short-term variations in surface elevation, which might explain the

higher differences between the IceBridge results and our 3-month temporally smoothed altimetry data. In contrast, the differences around the South Pole or in Queen Elizabeth Land (see also Fig. S6c) are significantly smaller. For the 2016 campaign of OIB, Brunt et al. (2018) furthermore report a spurious elevation variation of 10 to 15 cm across the wide-scan ATM swath, which indicates a bias in the instrumental tilt angle. This could explain the systematic differences along the 88°S circle profiles where this campaign is involved.

The observed  $\delta\Delta h$  can further be used to evaluate the uncertainty estimates. In Fig. 7c and f, the uncertainty estimates of the four contributing data sets are combined and compared to the observed differences. The comparison with both validation data sets supports the conclusion that the uncertainty estimates are reasonable. For  $\Delta h_{\text{ALT}}$  we expect higher errors in coastal regions due to the increased uncertainty of the topographic correction in radar altimetry. A similar relation to topography is expected for  $\Delta h_{\text{OIB}}$  due to the plane fit to the ATM point cloud, but surface roughness and crevassing also play an important role here. In contrast, the errors of the GNSS-derived  $\Delta h_{\text{KIN}}$  are almost independent of topography. Instead,  $\Delta h_{\text{KIN}}$  tends to be more uncertain on the plateau, where the soft snow causes large variations of the subsidence of the vehicles into the upper firn layers. The relatively low differences in  $\delta\Delta h$ , even in regions that imply a higher uncertainty, are likely just incidental for the small sample of validation data along the GNSS profiles.

In conclusion, this validation shows that remaining systematic biases (originating from satellite altimetry or the validation data) are less than a decimeter in the observed regions and that our uncertainty estimate is realistic. However, only altimetric SEC within the interval 2001–2016 can be validated in this way. For the earlier missions, no spatially extensive high-precision in situ data are publicly available.

## 4.2 Firn model

Another data set, which covers almost the identical spatial and temporal range as the altimetric data, is the IMAU Firn Densification Model (FDM; Ligtenberg et al., 2011), forced at the upper boundary by the accumulation and temperature of the Regional Atmospheric Climate Model, version 2.3p2 (van Wessem et al., 2018). The IMAU-FDM has been updated to the period 1979–2016, modeling the firn properties and the related surface elevation changes on a 27 km grid. However, as the FDM contains elevation anomalies only, any long-term elevation trend over 1979–2016, e.g., due to changes in precipitation on longer timescales (for example those observed in some regions of West Antarctica; Thomas et al., 2015) would not be included in the model. Furthermore, due to the nature of the model, it cannot give information about ice dynamic thinning and thickening. Hence, to compare the FDM and the SEC from altimetry, we first remove a linear trend from both data sets. This is performed

for the period 1992–2016 (depicted in Fig. S7). The trends are only calculated from epochs where both data sets have data; i.e., in the polar gap this comparison is limited to 2003–2016 or 2010–2016, depending on the first altimetry mission providing data here. After the detrending, the anomalies are used to calculate correlation coefficients for each cell, depicted in Fig. 8a. Figure 8b shows the average magnitude of the seasonal and interannual variations (nonlinear SEC), calculated as the rms of the anomalies from the altimetry data. Comparing the two maps shows that the correlation is around 0.5 or higher, except in regions where the magnitude of the anomalies is small (i.e., where the signal-to-noise ratio of the altimetric data is low) and where large accelerations in ice velocity are observed (such as near the grounding zone of Pine Island Glacier). The relationship between the correlation coefficient and the magnitude of the nonlinear SEC is depicted in Fig. 8c, where we see that for the vast majority of cells the correlation is positive. For anomalies with a nonlinear SEC  $> 0.5$  m, the average correlation is between 0.3 and 0.6.

Anomalies against the simultaneously observed long-term trend (1992–2016) can also be computed for earlier epochs. Assuming no significant changes in ice dynamics here, these anomalies allow for a comparison of Geosat and Seasat with the FDM. The median difference between the anomalies according to Geosat and the anomalies according to the FDM amounts to  $0.12 \pm 0.21$  m (see Fig. S8). Considering that this difference is very sensitive to extrapolating the long-term trends, this is a remarkable agreement. With a median of  $0.26 \pm 0.32$  m, the difference between anomalies from Seasat and from the FDM is larger, but this comparison is also more vulnerable to potential errors due to the extrapolation. As the FDM starts in 1979 while Seasat operated in 1978, we compare the Seasat data with the FDM anomalies from the respective months of 1979, which might impose additional differences. Finally, the FDM model has its own inherent errors and uncertainties. Therefore, only part of the differences originate from errors in the altimetry results.

## 5 Results

### 5.1 Surface elevation changes

The average rates of elevation change over different time intervals of our multi-mission time series are shown in Fig. 9. To calculate these rates, we first averaged the data over the first year and the last year of the interval to reduce the noise, then subtracted the respective averages from each other and finally divided these differences by their time difference in years. If one of the years does not cover the full annual cycle, we calculate the average only from the months covered in both years (July–October for 1978–2017, April–December for 1992–2017). We calculate the SEC rate from epoch differences instead of fitting a rate to all epochs because the first observations at specific latitudes start in different years,

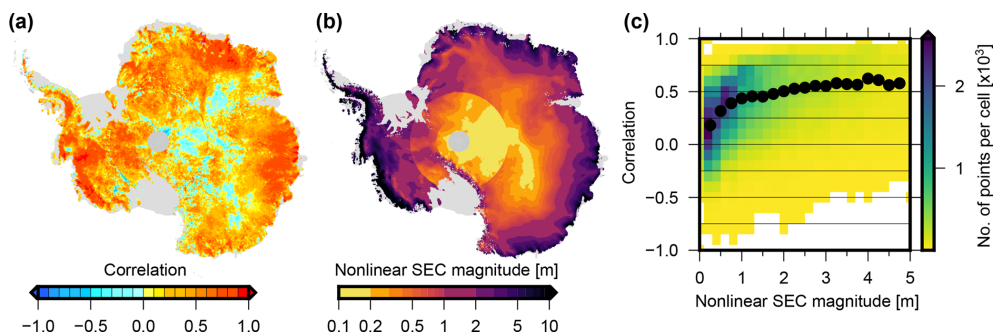


**Figure 8.** (a) Correlation coefficient between the SEC anomalies of the altimetry grids and the FDM over 1992–2016 after detrending. (b) Average magnitude of anomalies of the altimetry time series. (c) Correlation coefficient plotted against the nonlinear SEC. The point density is color coded from yellow to blue. The black dots show the binned mean values.

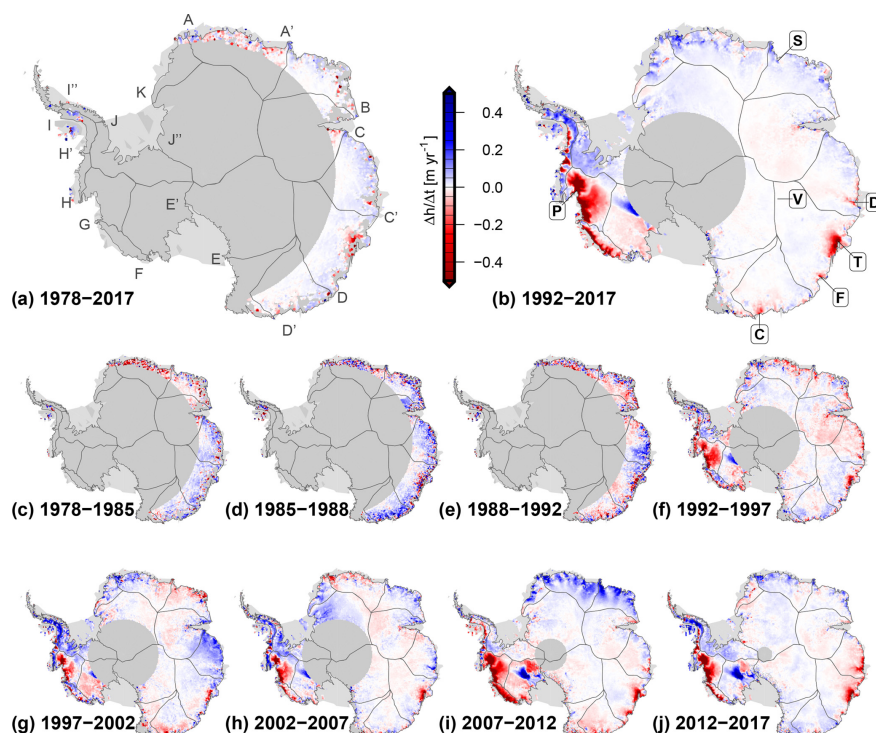


**Figure 9.** Multi-mission surface elevation change from the combined SEC time series over different time intervals. (a, b) The long-term surface elevation change between 1978 and 2017 and 1992 and 2017 for the covered area. (c–j) Elevation change over consecutive time intervals reveals the interannual variability. Thin lines mark the drainage basin outlines, denoted in panel (a). Bold letters in boxes in panel (b) denote areas mentioned in the text and in Fig. 10.

the observations have different precisions and the large gap between 1978 and 1985 is not covered by observations at all. These three points would lead to a bias towards the later epochs in a fit, so that the rates would not be representative for the true average elevation change over the full interval.

The long-term elevation changes over 25 years (Fig. 9b) show the well known thinning in the Amundsen Sea Embayment and at Totten Glacier, as well as the thickening of Kamb Ice Stream (see, e.g., Wingham et al., 2006b; Flament and Rémy, 2012; Helm et al., 2014). In contrast,

60 % of East Antarctica north of  $81.5^\circ$  S shows surface elevation changes of less than  $\pm 1 \text{ cm yr}^{-1}$ . Several coastal regions of the EAIS, however, show significant elevation changes. Totten Glacier (T in Fig. 9b) is thinning at an average rate of  $72 \pm 18 \text{ cm yr}^{-1}$  at the grounding line (cf. Fig. 10b). Several smaller glaciers in Wilkes Land also show a persistent thinning. We observe SEC rates of  $-26 \pm 10 \text{ cm yr}^{-1}$  at Denman Glacier (D),  $-41 \pm 19 \text{ cm yr}^{-1}$  at Frost Glacier (F) and  $-33 \pm 12 \text{ cm yr}^{-1}$  near Cook Ice Shelf (C). Rignot (2006) showed that the flow velocity of these glaciers, which are

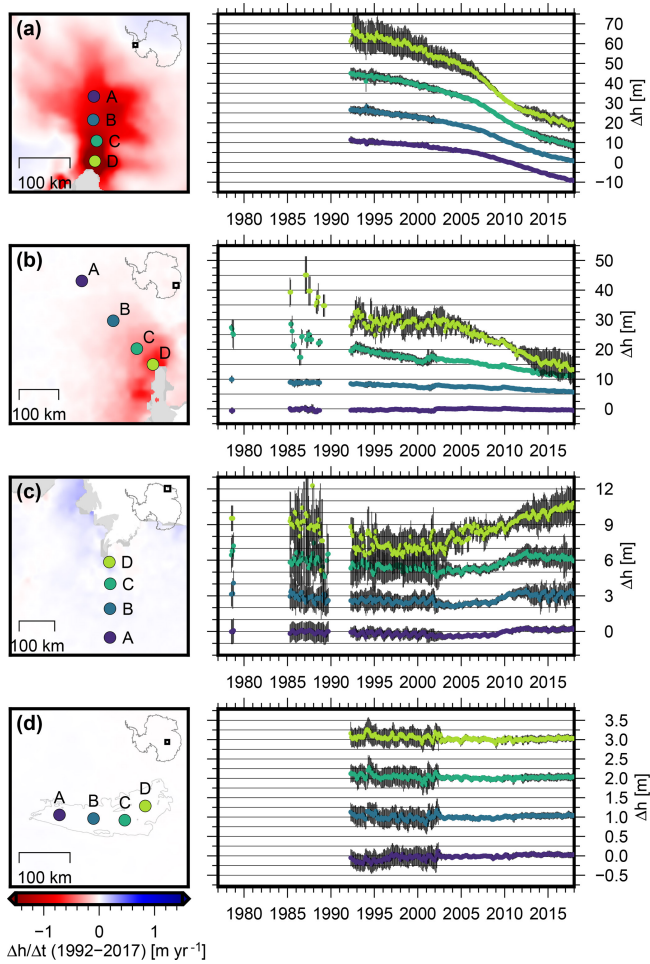


**Figure 10.** Multi-mission SEC time series in four selected regions (a) Pine Island Glacier, (b) Totten Glacier, (c) Shirase Glacier in Dronning Maud Land and (d) Lake Vostok (marked by P, T, S and V in Fig. 9b). The time series of points B, C and D are shifted along  $\Delta h$  for better visibility and the one  $\sigma$  uncertainty range is displayed in black. The maps on the left show the elevation change rate between 1992 and 2017 as in Fig. 9b (but in a different color scale).

grounded well below sea level, was above the balance velocity for many years. Miles et al. (2018) analyzed satellite images since 1973 and found that the flow velocity of Cook Ice Shelf glaciers has significantly accelerated since then. In contrast, the western sector of the EAIS (Coats Land, Dronning Maud Land and Enderby Land; basins J'-B) shows thickening over the last 25 years at rates of up to a decimeter per year.

Comparing the long-term elevation changes over 40 years (Fig. 9a) with those over 25 years shows the limitations of the early observations, but also the additional information they provide. There were relatively few successful observations at the margins. However, for Totten and Denman glaciers, the 40-year rates at a distance of approximately 100 km inland from the grounding line are similar to the rates over the

1992–2017 interval, which indicates a persistent rate of thinning. Another benefit of our merged time series is that they allow for the calculation of rates over any subinterval, independent of mission periods as demonstrated in Fig. 9c–j. For most of the coastal regions of the AIS, these rates over different intervals reveal that there is significant interannual variation. Such large-scale fluctuations in elevation change have been previously reported by Horwath et al. (2012) and Mémin et al. (2015) for the Envisat period. Our combined multi-mission time series now allow a detailed analysis of such signals on a temporal scale of up to 40 years.

Four examples for elevation change time series in the resulting multi-mission SEC grids are shown in Fig. 10 (coordinates in Table S2). Pine Island Glacier (PIG) is located in the Amundsen Sea Embayment, which is responsible for the largest mass losses of the Antarctic Ice Sheet (e.g., McMillan et al., 2014). In East Antarctica, the largest thinning rates are observed at Totten Glacier. The region of Dronning Maud Land and Enderby Land in East Antarctica has been chosen as an example for interannual variation. Here, Boening et al. (2012) reported two extreme accumulation events in 2009 and 2011, which led to significant mass anomalies. We chose a profile at Shirase Glacier as an example for this region. In contrast to the previous locations, a very stable surface elevation has been reported for Lake Vostok (e.g., Richter et al., 2014). This stability, however, has been a controversial case recently (Zwally et al., 2015; Scambos and Shuman, 2016; Richter et al., 2016). Therefore, our results in this region shall add further evidence that pinpoints the changes there.

For Pine Island Glacier (Fig. 10a), we observe a continuous thinning over the whole observational period since 1992 ( Seasat and Geosat measurements did not cover this region). Close to the grounding line (point D) the surface elevation has decreased by  $-45.8 \pm 7.8$  m since 1992, which means an average SEC rate of  $-1.80 \pm 0.31$  m  $\text{yr}^{-1}$ . The time series reveals that this thinning was not constant over time, but accelerated significantly around 2006. The mean rate at D over 1992–2006 of  $-1.32 \pm 0.66$  m  $\text{yr}^{-1}$  increased to  $-4.17 \pm 1.67$  m  $\text{yr}^{-1}$  over 2007–2010. After 2010, the thinning rates near the grounding line decelerate again and for the period 2013–2017, the rate at D of  $-1.31 \pm 0.80$  m  $\text{yr}^{-1}$  is very close to the rate preceding the acceleration. Also, at greater distances from the grounding line (B at 80 km, A at 130 km) we observe an acceleration of the prevailing rates around 2006 ( $-0.44 \pm 0.15$  m  $\text{yr}^{-1}$  over 1992–2006,  $-1.20 \pm 0.10$  m  $\text{yr}^{-1}$  over 2006–2017 at A). In contrast to the points near the grounding line, further inland the thinning has not decelerated so far and is still at a high level. Hence, for the most recent period (2013–2017) the elevation at all points along the 130 km of the main flow line is decreasing at very similar rates. A similar acceleration of the elevation change rate near the grounding line, followed by slowdown, is observed by Konrad et al. (2016). The onset of this acceleration coincides with the detaching of the ice shelf from a pinning point (Rignot et al., 2014). For the time after 2009, Joughin

et al. (2016) report relatively little grounding line migration, resulting in a leveling off of the ice flow velocity. This agrees with our observed slowdown of elevation changes.

For Totten Glacier in East Antarctica (Fig. 10b), we observe a clear negative SEC. This has been previously reported by several authors (e.g., Pritchard et al., 2009; Flament and Rémy, 2012; Zwally et al., 2015), but our data provide an unprecedented time span and temporal resolution, allowing for the analysis of the evolution of the elevation changes on a monthly scale over up to 40 years. At the grounding line (point D), Totten Glacier thinned by  $31.8 \pm 7.7$  m between 1987 and 2017, which results in an average SEC rate of  $-1.03 \pm 0.25$  m yr $^{-1}$ . Seasat could not provide successful observations at the grounding line, but the time series for point C (around 60 km inland) with a rate of  $-0.38 \pm 0.10$  m yr $^{-1}$  between 1978 and 2017 and for point B (150 km) with a rate of  $-0.11 \pm 0.04$  m yr $^{-1}$  indicate that this thinning preceded the epoch of Geosat. At point A in a distance of 280 km, we find no significant elevation change ( $0.01 \pm 0.03$  m yr $^{-1}$  for 1978–2017). The temporal resolution of these data allows us to analyze the change over time. While we see a significant thinning at the grounding line between 1987 and 1994 of  $16.6 \pm 9.8$  m, the elevation stabilized between 1994 and 2004 to within  $\pm 1.5$  m. After 2004, the ice at the grounding line thinned again by  $15.4 \pm 5.5$  m until 2017. Li et al. (2016) observe a similar variation in ice velocity measurements between 1989 and 2015. Combining their ice discharge estimates with surface mass balance, they obtain a relatively large mass imbalance for Totten Glacier in 1989, decreasing in the following years to a state close to equilibrium around 2000. After 2000, they observe an acceleration of ice flow, again consistent with our thinning rates. The authors attribute this high variability to variations in ocean temperature. In another study, Li et al. (2015) observe a grounding line retreat at Totten Glacier of 1 to 3 km between 1996 and 2013 using SAR interferometry. They conclude that this indicates a thinning by 12 m, which is again consistent with our results over this period ( $12.0 \pm 8.8$  m).

At Shirase Glacier in Dronning Maud Land (DML, Fig. 10c), we observe a relatively stable surface with a slightly negative change rate between 1978 and the early 2000s. The subintervals until 2002 in the elevation change maps of Fig. 9c–g confirm that this agrees with the large-scale trend in this region. After 2002, however, the rate changed significantly. Our time series show an increasing surface elevation, which is most pronounced during the time of the two significant accumulation events in 2009 and 2011 in this region (Boening et al., 2012; Lenaerts et al., 2013). At point C, the elevation changed by  $1.0 \pm 1.5$  m between 2008 and 2012. Even at point A, more than 200 km inland and at an altitude of 2500 m, the elevation increased by  $0.55 \pm 0.50$  m during this time. At point D, an abrupt elevation increase is also observed in 2003, which corresponds to another SMB anomaly (cf. Fig. 2a in Lenaerts et al., 2013).

The map in Fig. 9h shows that the coastal regions of Enderby Land (basins A–B) already experienced elevation gains before 2007. In contrast to the 2009 and 2011 events, which affected a very large region (Fig. 9i), this earlier accumulation event is significantly more localized at the coast.

In contrast to the regions discussed so far, the elevation change on the plateau of East Antarctica is very small. The time series for four different points at Lake Vostok (Fig. 10d) show rates within uncertainties and very close to zero (point A:  $5 \pm 9$  mm yr $^{-1}$ , B:  $-1 \pm 10$  mm yr $^{-1}$ , C:  $-3 \pm 9$  mm yr $^{-1}$ , D:  $-1 \pm 10$  mm yr $^{-1}$  between 1992 and 2017). The larger variations in the ERS time series are a result of the lower resolution of the waveform in the ice mode of the ERS satellites. These rates contradict the findings of Zwally et al. (2015). They report a surface elevation increase of 20 mm yr $^{-1}$  over Lake Vostok, which would result in an elevation increase of 0.5 m over the period 1992–2017. Our results are confirmed by ground-based static GNSS observations (Richter et al., 2008,  $0.3 \pm 4.9$  mm yr $^{-1}$ ), kinematic GNSS profiles measured around Vostok Station using snow mobiles (Richter et al., 2014,  $1 \pm 5$  mm yr $^{-1}$ ) and by GNSS profiles using traverse vehicles over the entire Lake Vostok region (Schröder et al., 2017,  $-1 \pm 5$  mm yr $^{-1}$ ).

## 5.2 Ice sheet mass time series

The surface elevation time series are converted into ice mass changes in order to determine their effect on global sea level. In the first step, the SECs are corrected for uplift rates related to glacial isostatic adjustment (GIA) using coefficients from the IJ05\_R2 model (Ivins et al., 2013). This GIA model predicts an uplift of 5 mm yr $^{-1}$  near the Antarctic Peninsula and rates between  $-0.5$  and  $+2$  mm yr $^{-1}$  in East Antarctica. Furthermore, we multiplied the SEC by a scaling factor  $\alpha = 1.0205$  to account for elastic solid earth rebound effects (Groh et al., 2012). The resulting ice sheet thickness changes are multiplied by each cell's area and a density according to a firn and ice mask (McMillan et al., 2014; McMillan et al., 2016), depicted in Fig. S10, to obtain a mass change. In regions where ice dynamic processes are assumed to be dominating (e.g., in the Amundsen Sea Embayment, Kamb Ice Stream or Totten Glacier), we use a density of  $917 \text{ kg m}^{-3}$ . Elsewhere, we apply the density of near-surface firn as modeled by Ligtenberg et al. (2011), using annual averages of accumulation, 10 m wind speed and surface temperature. We have chosen this straightforward method here, instead of using the modeled impact of the temporal variations of accumulation, melting and firn compaction on the firn layer (see, e.g., Zwally et al., 2015; Kallenberg et al., 2017) in the volume-to-mass conversion. This allows us to keep our altimetry time series independent of the modeled variations in SMB, which is a prerequisite for the interpretation of the comparison of both data sets.

We integrate our measurements over larger regions to calculate the cumulative mass anomalies for individual drainage

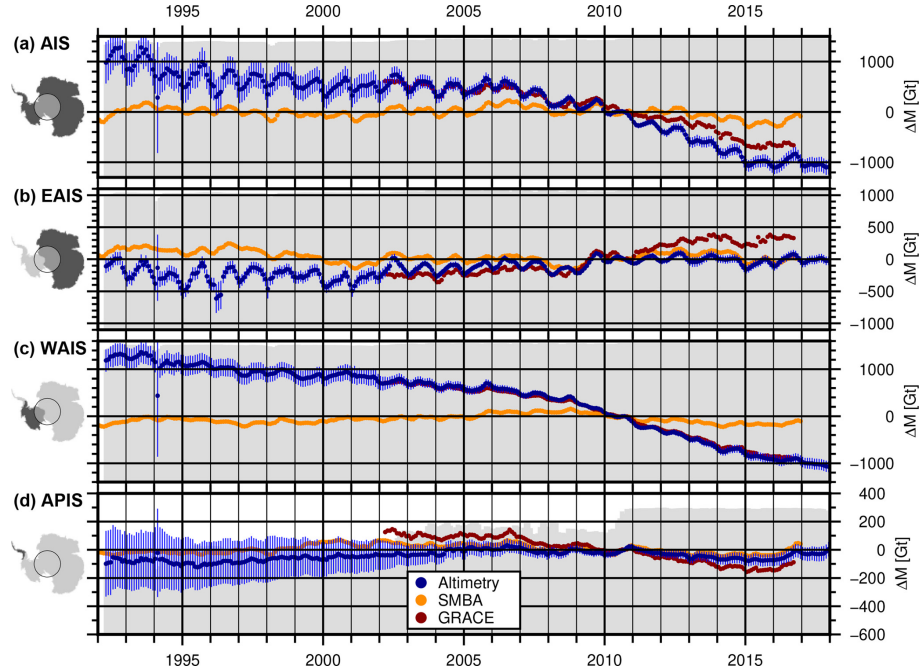


**Figure 11.** Mass change of the Antarctic Ice Sheet north of  $81.5^{\circ}$  S **(a)** and the three subregions **(b:** EAIS, **c:** WAIS and **d:** APIS) from our combined altimetric time series (blue), GRACE (red) and SMBA (orange). The error bars show the uncertainty estimate  $\sigma_{\Sigma}$  of the altimetry data according to Sect. S6.2. The gray color in the background displays the fraction of the area covered by altimetry (up to the top of the panel means 100 %).

basins and major Antarctic sectors (AIS; WAIS; EAIS; APIS). Our basin delineations are from Rignot et al. (2011), which have been updated for the second Ice Sheet Mass Balance Inter-comparison Exercise (IMBIE-2; Shepherd et al., 2018). Cells that were masked out due to the predominance of rocks or that are considered unobserved after our gridding (due to the polar gap or a lack of valid observations) are not included in these sums. Uncertainty estimates are obtained by propagating the uncertainties of the SEC, the GIA and the firn density to the basin sums for each month (see Sect. S6.2 for details). To account for the lack of information due to unobserved cells, we also add a total estimate for the effect of these cells, based on trends from GRACE, to the error budget.

Figure 11a–d show time series for the entire AIS north of  $81.5^{\circ}$  S (i.e., covered by satellite altimetry since 1992), and the subregions EAIS, WAIS and the APIS. Similar time series for the single drainage basins over 1992–2017 are shown in Fig. 12. For the coastal areas of the EAIS the full time interval since 1978 is shown in Fig. 13. These 4-decade time series use data north of  $72^{\circ}$  S only and, hence, provide a nearly consistent observational coverage over the whole period. To support the interpretation and evaluate the temporal evolution, we compared the respective time series to GIA-corrected cumulated mass anomalies from satellite gravimetry (GRACE; Groh and Horwath, 2016), which are products of the ESA Climate Change Initiative (CCI) Antarctic Ice

Sheet project and are available for download at [https://data1.geo.tu-dresden.de/ais\\_gmb](https://data1.geo.tu-dresden.de/ais_gmb) (last access: 1 February 2019) and <http://cci.esa.int/data> (last access: 1 February 2019). To reduce the effect of noise in the GRACE monthly solutions and to make the data more comparable to our altimetry results, we applied a 3-month moving average to the GRACE time series. We also compare our data to time series of cumulated surface mass balance anomaly (SMBA) from RACMO2.3p2 (van Wessem et al., 2018). To obtain these anomalies, the gridded SMB rates have been reduced by a mean rate and integrated over time. Similar to the IMAU firn model, these SMBAs contain seasonal and interannual variations due to surface processes but do not include long-term changes over the full modeled period (1979–2016). The different time series show the good agreement of the techniques in resolving interannual variations. For example for the basin of Totten Glacier (C’–D in Fig. 12), all techniques observe a negative mass anomaly in early 2008, followed by a significant mass gain in 2009 as previously reported by Velicogna et al. (2014) and Li et al. (2016). Between the epochs 03/2008 and 10/2009, we obtain a mass difference of  $116.6 \pm 27.0$  Gt from altimetry, 109.4 Gt from SMBA and 113.4 Gt from GRACE. The high agreement with SMBA indicates that this mass gain at Totten Glacier is caused by snow accumulation. In most of the basins, we observe a similar high agreement in the short-term variations. A good example for a total mass change signal which is constituted

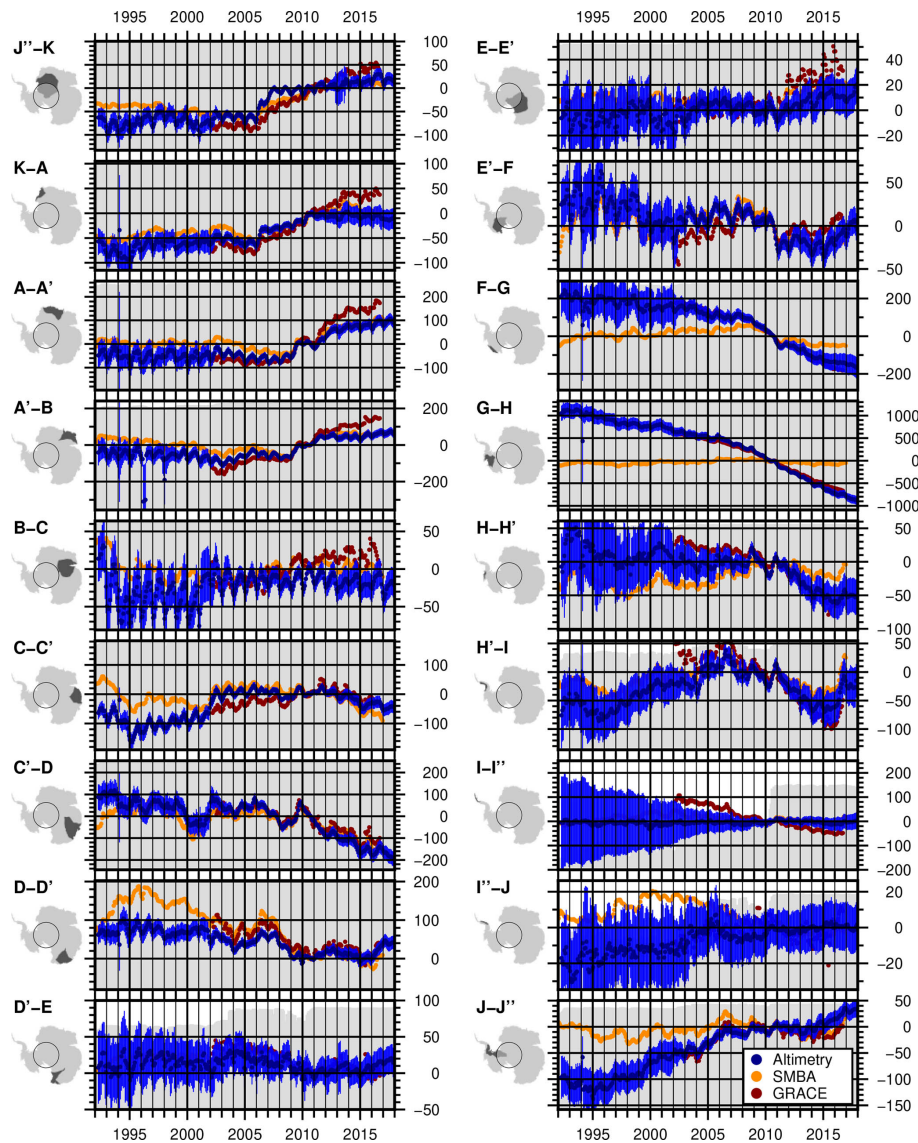


**Figure 12.** Mass change ( $\Delta M$  [Gt]) of the individual drainage basins north of  $81.5^\circ$  S from our combined altimetric time series (blue), GRACE (red) and SMBA (orange). The error bars show the uncertainty estimate  $\sigma_\Sigma$  of the altimetry data according to Sect. S6.2. The gray color in the background displays the fraction of the area covered by altimetry (the top of each panel means 100 %).

from components of SMBA and ice dynamics is the Getz and Abbot region (F–G) in West Antarctica. While all techniques observe a significant mass loss between 2009 and 2011, the SMBA does not contain the decadal trend, as observed by altimetry and GRACE. In some regions, there are also significant discrepancies between the data sets of satellite altimetry and GRACE. Inadequate sampling by radar altimetry (such as in the northern tip of the Antarctic Peninsula (I–I'') where steep regional topography and small outlet glacier size limits the recovery), leakage in the GRACE estimate between different sectors and uncertainties in the individual measurements and in the geophysical corrections might cause these differences. In George V Land (D–D'), the agreement during the GRACE period is reasonable, while the mass gain,

indicated by SMBA in the early 1990s, is not revealed by the altimetry time series.

Over the last 25 years our data indicate a clearly negative mass balance of  $-2068 \pm 377$  Gt for the AIS (Fig. 11a), which corresponds to an increase in mean sea level of  $5.7 \pm 1.0$  mm. This change is mainly a result of the mass loss in the WAIS over the last decade. In contrast, the EAIS has been very stable over our observational record ( $120 \pm 121$  Gt between 1992 and 2017). The time series of the APIS contains large uncertainties due to many unobserved cells. Mass change rates for selected regions, obtained from the differences over a specific time interval, and their uncertainties are given in Table 2. We calculated separate trends for the area north of  $72^\circ$  S, which is covered by all satellites, the area

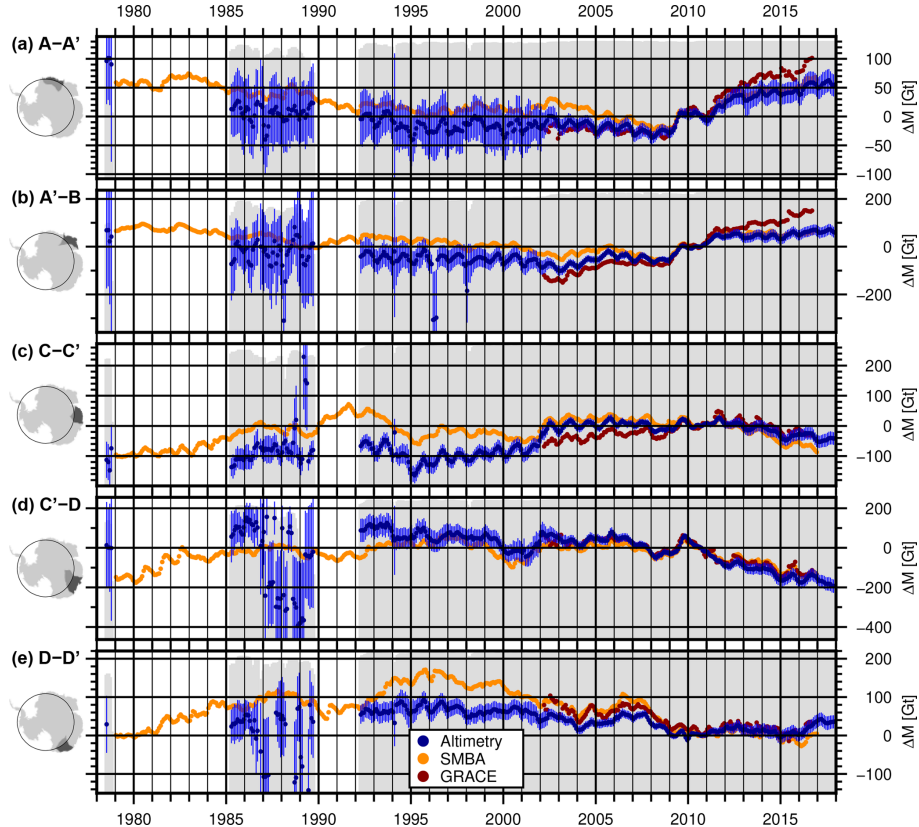


**Figure 13.** Mass change of subregions north of  $72^{\circ}$  S for several East Antarctic drainage basins from our combined altimetric time series (blue), GRACE (red) and SMBA (orange). The error bars show the uncertainty estimate  $\sigma_{\Sigma}$  of the altimetry data according to Sect. S6.2. The gray color in the background displays the fraction of the area covered by altimetry (the top of each panel means 100 %).

north of  $81.5^{\circ}$  S, which has been covered since the launch of ERS-1, and for the total area, which has been covered since the launch of CryoSat-2, except for its 500 km polar gap. A total of 96.4 % of the cells classified as ice sheet north of  $81.5^{\circ}$  S are successfully covered by observations of ERS-1. Cells without successful observation occur mostly at the APIS, where only 61 % is covered with data.

From the overall mass loss of  $-2068 \pm 377$  Gt for the AIS ( $< 81.5^{\circ}$  S over 1992–2017) we obtain an average long-term rate of  $-84.7 \pm 15.5$  Gt yr $^{-1}$  (or a corresponding mean sea level change rate of  $0.24 \pm 0.04$  mm yr $^{-1}$ ). After 2010, this rate accelerated to  $-137 \pm 25$  Gt yr $^{-1}$  or  $0.38 \pm 0.07$  mm yr $^{-1}$  of mean sea level.

## 6 Discussion

### 6.1 Surface elevation changes

Combining all the single missions consistently, our SEC time series allow for the analysis of the long-term changes over the full time period of satellite altimetry observations. For 79 % of the area of the AIS, this means a time span of 25 years. Over 25 % of the ice sheet, largely in the coastal

regions of East Antarctica, the time series can be extended back 40 years. Such long-term trends are significantly less affected by short-term variations in snowfall than a trend from a single mission. Furthermore, the period of observation of a single mission is short compared to climatic oscillations as reported by, e.g., Mémin et al. (2015). Our extended time series helps to separate elevation change due to climate variations from potentially accelerating volume losses. Seasat and Geosat also provide important information here, despite their larger uncertainties. Due to the stability criteria in the calibration, we do not expect significant new insights on the East Antarctic Plateau (even as regional variation still may be discernible as we used an ice-sheet-wide average in calibration). However, in the coastal regions of East Antarctica, with SECs of up to several meters with respect to 2010 (see Fig. 6), the older data can also contribute significant information to the study of elevation changes in a long-term context of 40 years (cf. the rates in Fig. 9 and their uncertainties in Fig. S9). Unfortunately, in coastal DML west of the ice divide A', the data of Seasat and Geosat are very noisy due to the mountain ranges just north of  $72^{\circ}$  S in these regions. They lead to many signal losses across this part of the ice sheet. The same applies to the measurements at the APIS.

**Table 2.** Mass change rates for different regions of the Antarctic Ice Sheet and different time intervals. The sizes of the total and observed area refer to all cells classified as ice sheet in the respective region (and if stated are limited by the given latitude).

Region	Area [ $10^3 \text{ km}^2$ ]		$dM/dt [\text{Gt yr}^{-1}]$				
	Total	Observed	1978–2017	1992–2017	1978–1992	1992–2010	2010–2017
AIS	11 892	11 630	–	–	–	–	$-117.5 \pm 25.5$
EAIS	9620	9413	–	–	–	–	$1.6 \pm 13.1$
WAIS	2038	2008	–	–	–	–	$-114.5 \pm 19.9$
APIS	232	208	–	–	–	–	$-4.5 \pm 8.7$
AIS (< 81.5° S)	9391	9053	–	$-84.7 \pm 15.5$	–	$-58.6 \pm 20.3$	$-137.0 \pm 24.9$
EAIS (< 81.5° S)	7764	7555	–	$4.9 \pm 5.0$	–	$8.0 \pm 6.2$	$2.4 \pm 12.4$
WAIS (< 81.5° S)	1394	1358	–	$-91.7 \pm 10.3$	–	$-69.4 \pm 13.1$	$-134.9 \pm 19.6$
APIS (< 81.5° S)	232	142	–	$2.1 \pm 8.9$	–	$2.8 \pm 12.3$	$-4.5 \pm 8.7$
EAIS (< 72° S)	2779	2274	$1.5 \pm 5.8$	$-3.4 \pm 4.0$	$12.1 \pm 17.4$	$0.0 \pm 4.9$	$-8.4 \pm 10.1$

For the APIS (< 72° S), the very sparse observations of Seasat and Geosat did not allow for the calculation of a reliable trend.

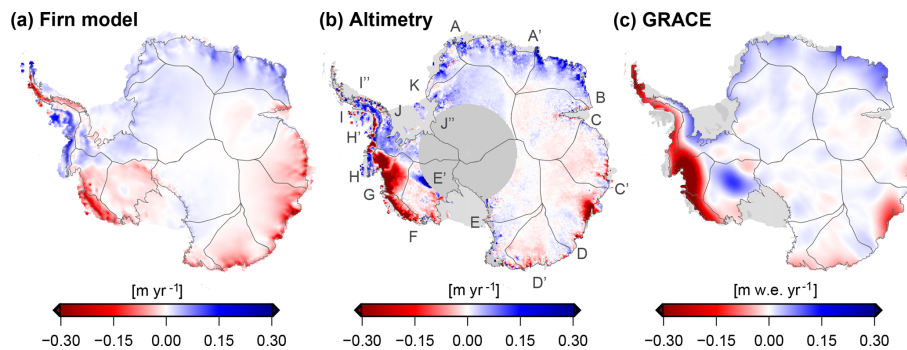


**Figure 14.** Mean rates for the time interval 2002–2016 of elevation changes from IMAU-FDM (a), from the multi-mission SEC grids (b) and of the mass changes from GRACE (c).

The benefits of a seamless combination of the time series are demonstrated in Fig. 9. The time intervals for the elevation changes are independent of the observational period of a single mission. This is necessary to analyze processes which occurred close to the transition between different missions. A good example of the advantage of such long time series is the elevation changes caused by the accumulation events in DML. Figure 10c clearly shows the changes in elevation, caused by the strong snowfall events in 2009 and 2011. The mission lifetime of ICESat ended during epoch 10/2009, CryoSat-2 provided the first measurements in epoch 07/2010. Only Envisat covered both events, but here the orbit was shifted in epoch 10/2010, resulting in different repeat-track cells covered before and after the orbit shift. We merged all these missions as described in Sect. 3.3, which allows us to analyze the full time series. Comparing the elevation changes from altimetry with those in the FDM serves as a cross-validation of both data sets. For example, at point A in Fig. 10c our SEC time series observes a change of  $0.55 \pm 0.50 \text{ m}$  between 2008 and 2012, while the FDM mod-

els a very similar elevation gain of  $0.48 \text{ m}$  for this period. Figure 8 shows the degree of agreement over the entire AIS.

As these elevation change rates alone do not contain any information on their origin, additional data are needed for improved process understanding. Figure 14 shows SEC rates for the interval 2002–2016 (calculated as in Sect. 5.1 over March–September, respectively) from altimetry and the IMAU-FDM and corresponding rates of ice mass changes from GRACE. These maps show that the elevation gains in DML and Enderby Land agree very well with the firn model, which implies that increased snow accumulation during this period is responsible for the thickening. For Princess Elizabeth Land (C–C'), the negative rates agree as well, implying that the thinning here can be related to lower than normal snow accumulation. In contrast, the strong thinning along the Amundsen Sea Embayment (G–H) or the thickening of Kamb Ice Stream (E'–F) is not present in the FDM results but does show up in the GRACE data. Due to the higher densities of the involved material, ice dynamic processes are even more pronounced in the map of mass changes compared to the maps of elevation changes.

The inland propagation of dynamic thinning of the glaciers of the Amundsen Sea Embayment over the last few decades has been described by Konrad et al. (2016). A recent onset of significant mass losses has also been reported for the adjacent glaciers along the Bellingshausen Sea (H–I; Wouters et al., 2015) and on the Getz and Abbot region (F–G; Chuter et al., 2017). Figure 9i reveals that the largest losses along the coast of the WAIS occurred between 2007 and 2012. The period 2012–2017 (Fig. 9i) shows that only a part of these large rates is persistent. While the ice discharge of the Getz and Abbot region increased by 6 % between 2008 and 2015 (Gardner et al., 2018), the deceleration of the elevation change after 2012 indicates that interannual variations in SMB also have to be considered here (see also Chuter et al., 2017). The FDM-derived rate in Fig. 14a confirms the role of the surface mass balance in this region.

## 6.2 Ice sheet mass time series

The integrated time series of basin-wide mass changes allow for the analysis of the temporal evolution at a monthly resolution (Fig. 12). As described in the previous section, for most of the basins of the WAIS, they show an increase of mass loss after the mid-2000s. The acceleration of thinning at the Getz and Abbot region (F–G) started already in 2004, but experienced a further significant acceleration after 2007. In the Amundsen Sea Embayment, a small positive mass anomaly in late 2005 relates to a similar event in the SMBA time series, but after that, also here the overall mass losses accelerated. The Bellingshausen Sea basin (H–H') was relatively stable until 2009, but started to lose significant amounts of mass after that time, as reported by Wouters et al. (2015). Since 2016, however, we observe that the basins at the Bellingshausen Sea and the western part of the peninsula regained mass. The comparison with SMBA reveals that this can be explained by a positive snowfall anomaly in this area in 2016. The shape and orientation of the peninsula makes GRACE observations challenging with respect to leakage and GRACE error effects (Horwath and Dietrich, 2009). Nevertheless, the results of the satellite gravity mission confirm this mass anomaly.

A similar comparison of the ice-sheet-wide mass time series between altimetry and GRACE in Fig. 11 reveals that for the entire WAIS, both data sets agree very well, while for the APIS and the EAIS, we observe significant differences on a decadal scale of the trends. The percentage of observed area of the APIS (gray area in the background of Fig. 11d) indicates that before 2010, a significant part of the area remained unobserved. Here, conventional RA measurements very often failed due to the rugged terrain. Even for ICE-Sat, the large across-track distances and the dependence on cloud-free conditions make measurements very sparse at the peninsula. With the weather independent, dense and small footprint measurements of CryoSat-2 in SARIn mode, up to 80 % of the area is covered by observations. Compared to

GRACE, however, we observe a significantly weaker mass loss signal. Thomas et al. (2008) pointed out that RA fails to sample the large elevation changes in narrow valleys of outlet glaciers. This leads to an overall underestimation of the signal by altimetric observations. Furthermore, the complex terrain, especially in the APIS, also causes problems in the parameter fit. Even if enough valid measurements are available (as from, for example, ICESat or CryoSat-2), the fit of a planar surface over a diameter of 2 km in our repeat-altimetry processing can hardly adequately represent the real topography here. Our approach is designed to provide valid results over the majority of the AIS. Under the challenging conditions of the APIS, modifications such as a smaller diameter or more complex parameterization of the surface would surely help to improve the results. Furthermore, we did not calculate a SEC for cells that are further away than a beam-limited radar footprint from valid measurements. In order to interpolate or even extrapolate the results to unobserved cells, advanced gridding methods such as kriging, especially with the help of additional data sets (Hurkmans et al., 2012), would be advisable.

This effect may also explain the differences of our results, compared to the results of the combination of different techniques by Shepherd et al. (2018). Their 1992–2017 rate of  $-109 \pm 56 \text{ Gt yr}^{-1}$  agrees within error bars with our results, but our rate of  $-84.7 \pm 15.5 \text{ Gt yr}^{-1}$  is considerably smaller. Part of this disagreement might be attributed to differences in the estimates for the Antarctic Peninsula where retrieving reliable radar altimetry estimates is non-trivial. However, the extended material in Shepherd et al. (2018) shows that there are still some discrepancies between the different techniques to determine the AIS mass balance. For the time interval 2003–2010 (Extended Data Table 4 in Shepherd et al., 2018) the input–output method obtains a rate of  $-201 \pm 82 \text{ Gt yr}^{-1}$  for the AIS, while the mass balance rates from satellite gravimetry ( $-76 \pm 20 \text{ Gt yr}^{-1}$ ) and from altimetry ( $-43 \pm 21 \text{ Gt yr}^{-1}$ ) agree much better with our result for the AIS ( $< 81.5^\circ \text{ S}$ ) between 2003 and 2010 of  $-65 \pm 25 \text{ Gt yr}^{-1}$ .

Besides the peninsula, our comparison of mass changes from altimetry and from GRACE at the EAIS (Fig. 11b) reveals some significant differences between the time series. For the time interval 2002 to 2016 (see Sect. S6.3), the mean rate at the EAIS from altimetry ( $9.6 \pm 6.9 \text{ Gt yr}^{-1}$ ) is mainly dominated by the accumulation events in 2009 and 2011. In contrast, the GRACE data imply an average mass gain of  $42.1 \text{ Gt yr}^{-1}$  over this time interval. Especially after 2011, the differences become very prominent in the time series. The mass changes for the individual basins (Fig. 12) reveal that this difference in the signals can be attributed to DML and Enderby Land. This might be a sign for dynamic thickening. Here, all elevation changes have been converted to mass using the density of surface firn. If a part of the positive elevation changes in this region were indeed caused by ice dynamics, this would lead to an underestimation of mass gains from

altimetry. The results of the Bayesian combined approach of Martín-Español et al. (2017) also suggest a small dynamic thickening in this region. Rignot et al. (2008) observed no significant mass changes in this region between 1992 and 2006 using the input–output method. Gardner et al. (2018) compared present-day ice flow velocities to measurements from 2008. They obtain a slightly reduced ice discharge in DML (which would support the hypothesis of a dynamic thickening), while they observe a small increase in discharge for Enderby Land. Part of the discrepancy with the GRACE results could be also due to uncertainties in the geophysical corrections applied to the GRACE data, such as the effects of glacial isostatic adjustment. More work, similar to the Ice Sheet Mass Balance Inter-comparison Exercises (Shepherd et al., 2018), or the combination of different types of observations as in Martín-Español et al. (2016), could help identify the reasons leading to the disagreement.

## 7 Conclusions

In this paper we presented an approach to combine different satellite altimetry missions, observation modes and techniques. The reprocessing of the conventional pulse-limited radar altimetry ensures that two fundamental steps in processing of radar ice altimetry, the waveform retracking and the slope correction, are performed consistently. Furthermore, we showed that the methods used here improved the overall precision by 50 % over the standard data sets available from ESA and NASA. The validation with in situ and airborne measurements and the comparison with the IMAU-FDM shows that inter-mission offsets have been successfully corrected and that the uncertainty estimates for our resulting monthly multi-mission SEC grids are realistic.

We analyzed the resulting time series and found that they provide detailed insight in the evolution of the surface elevation of the Antarctic Ice Sheet. From the combined SEC time series we calculated the long-term surface elevation change over the last 25 years. Observations from the Seasat and Geosat missions extend the time series in the coastal regions of East Antarctica back to 1978. The unique data show that large parts of the East Antarctic Plateau are very close to equilibrium, while changes over shorter time intervals identify interannual variations, which cannot be identified in long-term trends and are mostly associated with snowfall anomalies.

The monthly mass time series show that the AIS (excluding the polar gap within  $81.5^{\circ}$  S) lost an average amount of mass of  $-84.7 \pm 15.5 \text{ Gt yr}^{-1}$  between 1992 and 2017 (equivalent to  $0.24 \pm 0.04 \text{ mm yr}^{-1}$  of mean sea level change). These losses accelerated in several regions and, hence, for 2010–2017 we obtain  $-137.0 \pm 24.9 \text{ Gt yr}^{-1}$  (or  $0.38 \pm 0.07 \text{ mm yr}^{-1}$ ) for the same area. The comparison of the altimetry-derived mass changes, integrated over different basins and regions of the ice sheet, with SMBA and GRACE

shows high consistency of the different techniques. A correlation coefficient between the mass anomalies from altimetry and from GRACE of 0.96 (for the time interval 2002–2016; see Table S4) indicates the excellent agreement of the observed interannual variations. The correlation with the SMBA (0.60 for 1992–2016) is comparatively lower but still indicates a high agreement. In the APIS, differences between the mass time series of the different techniques arise mainly due to the poor spatial sampling of the altimetry data, while for the EAIS, the remaining discrepancies to mass time series from GRACE might be explained by the density mask used or uncertainties in the GRACE processing. These remaining issues and open questions should be addressed in future work in order to further reduce the uncertainty of the estimates of the mass balance of the AIS. The recently launched laser altimeter ICESat-2 promises a new milestone in ice sheet altimetry. We believe that our multi-mission combination approach can provide an important tool for including the extremely high resolution of this mission into the long-time observations of satellite altimetry spanning the past few decades.

*Data availability.* Our resulting monthly  $10 \text{ km} \times 10 \text{ km}$  grids of SEC with respect to epoch 09/2010, accompanied by corresponding uncertainty estimates, are available for download at <https://doi.pangaea.de/10.1594/PANGAEA.897390> (Schröder et al., 2019).

*Supplement.* The supplement related to this article is available online at: <https://doi.org/10.5194/tc-13-427-2019-supplement>.

*Author contributions.* LS designed the study and developed the PLRA reprocessing, the repeat-altimetry processing and the time series generation. VH supplied the reprocessed CryoSat-2 SARIn data. SRML and MRvB provided the RACMO and IMAU-FDM models. All authors discussed the results and contributed to the writing and editing of the manuscript.

*Competing interests.* Michiel van den Broeke is a member of the editorial board of the journal. All other authors declare that they have no conflict of interest.

*Acknowledgements.* This work is supported by the Deutsche Bundesstiftung Umwelt (DBU, German Federal Environmental Foundation) and the German Ministry of Economics and Technology (grant 50EE1331 to Veit Helm). We thank the European Space Agency, the National Snow and Ice Data Center and the NASA Goddard Space Flight Center for providing the altimetry data products. We would especially like to thank Jairo Santana for his support in accessing the GSFC data. We are very grateful for the comments from the anonymous referees, Andrew Shepherd and the editor Etienne Berthier, which significantly helped to improve and clarify the manuscript. We acknowledge support by the Open

## References

- Adusumilli, S., Fricker, H. A., Siegfried, M. R., Padman, L., Paolo, F. S., and Ligtenberg, S. R. M.: Variable Basal Melt Rates of Antarctic Peninsula Ice Shelves, 1994–2016, *Geophys. Res. Lett.*, 45, 4086–4095, <https://doi.org/10.1002/2017GL076652>, 2018.
- Arthern, R., Wingham, D., and Ridout, A.: Controls on ERS altimeter measurements over ice sheets: Footprint-scale topography, backscatter fluctuations, and the dependence of microwave penetration depth on satellite orientation, *J. Geophys. Res.-Atmos.*, 106, 33471–33484, <https://doi.org/10.1029/2001JD000498>, 2001.
- Baarda, W.: A testing procedure for use in geodetic networks, Netherlands Geodetic Commission, Delft, the Netherlands, 1968.
- Bamber, J.: Ice Sheet Altimeter Processing Scheme, *Int. J. Remote Sens.*, 14, 925–938, <https://doi.org/10.1080/01431169408954125>, 1994.
- Bamber, J. L., Gomez-Dans, J. L., and Griggs, J. A.: A new 1 km digital elevation model of the Antarctic derived from combined satellite radar and laser data – Part 1: Data and methods, *The Cryosphere*, 3, 101–111, <https://doi.org/10.5194/tc-3-101-2009>, 2009.
- Boening, C., Lebsack, M., Landerer, F., and Stephens, G.: Snowfall-driven mass change on the East Antarctic ice sheet, *Geophys. Res. Lett.*, 39, L21501, <https://doi.org/10.1029/2012GL053316>, 2012.
- Brenner, A., Bindschadler, R., Zwally, H., and Thomas, R.: Slope-induced errors in radar altimetry over continental ice sheets, *J. Geophys. Res.*, 88, 1617–1623, <https://doi.org/10.1029/JC088iC03p01617>, 1983.
- Brenner, A., DiMarzio, J., and Zwally, H.: Precision and Accuracy of Satellite Radar and Laser Altimeter Data Over the Continental Ice Sheets, *IEEE T. Geosci. Remote*, 45, 321–331, <https://doi.org/10.1109/TGRS.2006.887172>, 2007.
- Brockley, D., Baker, S., Femenias, P., Martinez, B., Massmann, F.-H., Otten, M., Paul, F., Picard, B., Prandi, P., Roca, M., Rudenko, S., Scharroo, R., and Visser, P.: REAPER: Reprocessing 12 Years of ERS-1 and ERS-2 Altimeters and Microwave Radiometer Data, *IEEE T. Geosci. Remote*, 55, 5506–5514, <https://doi.org/10.1109/TGRS.2017.2709343>, 2017.
- Brunt, K. M., Hawley, R. L., Lutz, E. R., Studinger, M., Sonntag, J. G., Hofton, M. A., Andrews, L. C., and Neumann, T. A.: Assessment of NASA airborne laser altimetry data using ground-based GPS data near Summit Station, Greenland, *The Cryosphere*, 11, 681–692, <https://doi.org/10.5194/tc-11-681-2017>, 2017.
- Brunt, K. M., Neumann, T. A., and Larsen, C. F.: Assessment of altimetry using ground-based GPS data from the 88S Traverse, Antarctica, in support of ICESat-2, *The Cryosphere Discuss.*, <https://doi.org/10.5194/tc-2018-160>, in review, 2018.
- Chuter, S., Martín-Español, A., Wouters, B., and Bamber, J.: Mass balance reassessment of glaciers draining into the Abbot and Getz Ice Shelves of West Antarctica: Getz and Abbot Mass Balance Reassessment, *Geophys. Res. Lett.*, 44, 7328–7337, <https://doi.org/10.1002/2017GL073087>, 2017.
- Davis, C.: A Combined Surface/volume Scattering Retracking Algorithm for Ice Sheet Satellite Altimetry, in: *Geoscience and Remote Sensing Symposium, 1992, IGARSS '92. International*, Houston, TX, USA, 26–29 May 1992, vol. 2, 969–971, <https://doi.org/10.1109/IGARSS.1992.578311>, 1992.
- Davis, C.: A robust threshold retracking algorithm for measuring ice-sheet surface elevation change from satellite radar altimeters, *IEEE T. Geosci. Remote*, 35, 974–979, <https://doi.org/10.1109/36.602540>, 1997.
- Davis, C. and Ferguson, A.: Elevation change of the Antarctic ice sheet, 1995–2000, from ERS-2 satellite radar altimetry, *IEEE T. Geosci. Remote*, 42, 2437–2445, <https://doi.org/10.1109/TGRS.2004.836789>, 2004.
- Flament, T. and Rémy, F.: Dynamic thinning of Antarctic glaciers from along-track repeat radar altimetry, *J. Glaciol.*, 58, 830–840, <https://doi.org/10.3189/2012JoG11J118>, 2012.
- Frappart, F., Legrésy, B., Niño, F., Blarel, F., Fuller, N., Fleury, S., Birol, F., and Calmant, S.: An ERS-2 altimetry reprocessing compatible with ENVISAT for long-term land and ice sheets studies, *Remote Sens. Environ.*, 184, 558–581, <https://doi.org/10.1016/j.rse.2016.07.037>, 2016.
- Fricker, H. and Padman, L.: Thirty years of elevation change on Antarctic Peninsula ice shelves from multimission satellite radar altimetry, *J. Geophys. Res.*, 117, C02026, <https://doi.org/10.1029/2011JC007126>, 2012.
- Fyke, J., Lenaerts, J. T. M., and Wang, H.: Basin-scale heterogeneity in Antarctic precipitation and its impact on surface mass variability, *The Cryosphere*, 11, 2595–2609, <https://doi.org/10.5194/tc-11-2595-2017>, 2017.
- Gardner, A. S., Moholdt, G., Scambos, T., Fahnestock, M., Ligtenberg, S., van den Broeke, M., and Nilsson, J.: Increased West Antarctic and unchanged East Antarctic ice discharge over the last 7 years, *The Cryosphere*, 12, 521–547, <https://doi.org/10.5194/tc-12-521-2018>, 2018.
- Groh, A. and Horwath, M.: The method of tailored sensitivity kernels for GRACE mass change estimates, General Assembly EGU, Vienna, Austria, 17–22 April 2016, *Geophys. Res. Abstr.*, 18, EGU2016–12065, 2016.
- Groh, A., Ewert, H., Scheinert, M., Fritzsche, M., Rülke, A., Richter, A., Rosenau, R., and Dietrich, R.: An Investigation of Glacial Isostatic Adjustment over the Amundsen Sea sector, West Antarctica, *Global Planet. Change*, 98–99, 45–53, <https://doi.org/10.1016/j.gloplacha.2012.08.001>, 2012.
- Helm, V., Humbert, A., and Miller, H.: Elevation and elevation change of Greenland and Antarctica derived from CryoSat-2, *The Cryosphere*, 8, 1539–1559, <https://doi.org/10.5194/tc-8-1539-2014>, 2014.
- Hogg, A., Shepherd, A., Cornford, S., Briggs, K., Gourmelen, N., Graham, J., Joughin, I., Mouginot, J., Nagler, T., Payne, A., Rignot, E., and Wuite, J.: Increased ice flow in Western Palmer Land linked to ocean melting, *Geophys. Res. Lett.*, 44, 4159–4167, <https://doi.org/10.1002/2016GL072110>, 2017.
- Horwath, M. and Dietrich, R.: Signal and error in mass change inferences from GRACE: the case of Antarctica, *Geophys. J. Int.*, 177, 849–864, <https://doi.org/10.1111/j.1365-246X.2009.04139.x>, 2009.

- Horwath, M., Legréy, B., Rémy, F., Blarel, F., and Lemoine, J.-M.: Consistent patterns of Antarctic ice sheet interannual variations from ENVISAT radar altimetry and GRACE satellite gravimetry, *Geophys. J. Int.*, 189, 863–876, <https://doi.org/10.1111/j.1365-246X.2012.05401.x>, 2012.
- Hurkmans, R., Bamber, J., Sørensen, L., Joughin, I., Davis, C., and Krabill, W.: Spatiotemporal interpolation of elevation changes derived from satellite altimetry for Jakobshavn Isbræ, Greenland, *J. Geophys. Res.*, 117, F03001, <https://doi.org/10.1029/2011JF002072>, 2012.
- Ivins, E., James, T., Wahr, J., Schrama, E., Landerer, F., and Simon, K.: Antarctic contribution to sea level rise observed by GRACE with improved GIA correction, *J. Geophys. Res.-Sol. Ea.*, 118, 3126–3141, <https://doi.org/10.1002/jgrb.50208>, 2013.
- Joughin, I., Shean, D., Smith, B., and Dutrieux, P.: Grounding line variability and subglacial lake drainage on Pine Island Glacier, Antarctica, *Geophys. Res. Lett.*, 43, 9093–9102, <https://doi.org/10.1002/2016GL070259>, 2016.
- Kallenberg, B., Tregoning, P., Hoffmann, J. F., Hawkins, R., Purcell, A., and Allgeyer, S.: A new approach to estimate ice dynamic rates using satellite observations in East Antarctica, *The Cryosphere*, 11, 1235–1245, <https://doi.org/10.5194/tc-11-1235-2017>, 2017.
- Khvorostovsky, K.: Merging and Analysis of Elevation Time Series Over Greenland Ice Sheet From Satellite Radar Altimetry, *IEEE T. Geosci. Remote*, 50, 23–36, <https://doi.org/10.1109/TGRS.2011.2160071>, 2012.
- Konrad, H., Gilbert, L., Cornford, S., Payne, A., Hogg, A., Muir, A., and Shepherd, A.: Uneven onset and pace of ice-dynamical imbalance in the Amundsen Sea Embayment, West Antarctica, *Geophys. Res. Lett.*, 44, 910–918, <https://doi.org/10.1002/2016GL070733>, 2016.
- Lacroix, P., Dechambre, M., Legréy, B., Blarel, F., and Rémy, F.: On the use of the dual-frequency ENVISAT altimeter to determine snowpack properties of the Antarctic ice sheet, *Remote Sens. Environ.*, 112, 1712–1729, <https://doi.org/10.1016/j.rse.2007.08.022>, 2008.
- Legréy, B. and Rémy, F.: Altimetric observations of surface characteristics of the Antarctic ice sheet, *J. Glaciol.*, 43, 265–276, <https://doi.org/10.3189/S00221430000321X>, 1997.
- Legréy, B., Rémy, F., and Schaeffer, P.: Different ERS altimeter measurements between ascending and descending tracks caused by wind induced features over ice sheets, *Geophys. Res. Lett.*, 26, 2231–2234, <https://doi.org/10.1029/1999GL900531>, 1999.
- Legréy, B., Papa, F., Rémy, F., Vinay, G., van den Bosch, M., and Zanife, O.-Z.: ENVISAT radar altimeter measurements over continental surfaces and ice caps using the ICE-2 retracking algorithm, *Remote Sens. Environ.*, 85, 150–163, <https://doi.org/10.1016/j.rse.2004.11.018>, 2005.
- Legréy, B., Rémy, F., and Blarel, F.: Along track repeat altimetry for ice sheets and continental surface studies, in: Proc. Symposium on 15 years of Progress in Radar Altimetry, Venice, Italy, 13–18 March 2006, European Space Agency Publication Division, Noordwijk, the Netherlands, eSA-SP No. 614, paper No. 181, 2006.
- Lenaarts, J., van Meijgaard, E., van den Broeke, M., Ligtenberg, S., Horwath, M., and Isaksson, E.: Recent snowfall anomalies in Dronning Maud Land, East Antarctica, in a historical and future climate perspective, *Geophys. Res. Lett.*, 40, 2684–2688, <https://doi.org/10.1002/grl.50559>, 2013.
- Li, X., Rignot, E., Morlighem, M., Mouginot, J., and Scheuchl, B.: Grounding line retreat of Totten Glacier, East Antarctica, 1996 to 2013, *Geophys. Res. Lett.*, 42, 8049–8056, <https://doi.org/10.1002/2015GL065701>, 2015.
- Li, X., Rignot, E., Mouginot, J., and Scheuchl, B.: Ice flow dynamics and mass loss of Totten Glacier, East Antarctica, from 1989 to 2015, *Geophys. Res. Lett.*, 43, 6366–6373, <https://doi.org/10.1002/2016GL069173>, 2016.
- Li, Y. and Davis, C.: Decadal Mass Balance of the Greenland and Antarctic Ice Sheets from High Resolution Elevation Change Analysis of ERS-2 and Envisat Radar Altimetry Measurements, in: IEEE International Geoscience & Remote Sensing Symposium, IGARSS 2008, 8–11 July 2008, Boston, Massachusetts, USA, Proceedings, IEEE, 339–342, <https://doi.org/10.1109/IGARSS.2008.4779727>, 2008.
- Ligtenberg, S. R. M., Helsen, M. M., and van den Broeke, M. R.: An improved semi-empirical model for the densification of Antarctic firn, *The Cryosphere*, 5, 809–819, <https://doi.org/10.5194/tc-5-809-2011>, 2011.
- Martin, T., Zwally, H., Brenner, A., and Bindschadler, R.: Analysis and retracking of continental ice sheet radar altimeter waveforms, *J. Geophys. Res.*, 88, 1608, <https://doi.org/10.1029/JC088iC03p01608>, 1983.
- Martín-Español, A., Zammit-Mangion, A., Clarke, P., Flament, T., Helm, V., King, M., Lutcke, S., Petrie, E., Rémy, F., Schön, N., Wouters, B., and Bamber, J.: Spatial and temporal Antarctic Ice Sheet mass trends, glacio-isostatic adjustment and surface processes from a joint inversion of satellite altimeter, gravity and GPS data, *J. Geophys. Res.-Earth*, 121, 182–200, <https://doi.org/10.1002/2015JF003550>, 2016.
- Martín-Español, A., Bamber, J., and Zammit-Mangion, A.: Constraining the mass balance of East Antarctica, *Geophys. Res. Lett.*, 44, 4168–4175, <https://doi.org/10.1002/2017GL072937>, 2017.
- McMillan, M., Shepherd, A., Sundal, A., Briggs, K., Muir, A., Ridout, A., Hogg, A., and Wingham, D.: Increased ice losses from Antarctica detected by CryoSat-2, *Geophys. Res. Lett.*, 41, 3899–3905, <https://doi.org/10.1002/2014GL060111>, 2014.
- McMillan, M., Leeson, A., Shepherd, A., Briggs, K., Armitage, T., Hogg, A., Kuipers Munneke, P., van den Broeke, M., Noël, B., van de Berg, W., Ligtenberg, S., Horwath, M., Groh, A., Muir, A., and Gilbert, L.: A high-resolution record of Greenland mass balance, *Geophys. Res. Lett.*, 43, 7002–7010, <https://doi.org/10.1002/2016GL069666>, 2016.
- Mémin, A., Flament, T., Alizier, B., Watson, C., and Rémy, F.: Interannual variation of the Antarctic Ice Sheet from a combined analysis of satellite gravimetry and altimetry data, *Earth Planet. Sc. Lett.*, 422, 150–156, <https://doi.org/10.1016/j.epsl.2015.03.045>, 2015.
- Michel, A., Flament, T., and Rémy, F.: Study of the Penetration Bias of ENVISAT Altimeter Observations over Antarctica in Comparison to ICESat Observations, *Remote Sensing*, 6, 9412–9434, <https://doi.org/10.3390/rs6109412>, 2014.
- Miles, B. W. J., Stokes, C. R., and Jamieson, S. S. R.: Velocity increases at Cook Glacier, East Antarctica, linked to ice shelf loss and a subglacial flood event, *The Cryosphere*, 12, 3123–3136, <https://doi.org/10.5194/tc-12-3123-2018>, 2018.

- Mouginot, J., Rignot, E., and Scheuchl, B.: Sustained increase in ice discharge from the Amundsen Sea Embayment, West Antarctica, from 1973 to 2013, *Geophys. Res. Lett.*, 41, 1576–1584, <https://doi.org/10.1002/2013GL059069>, 2014.
- Nilsson, J., Vallelonga, P., Simonsen, S., Sørensen, L., Forsberg, R., Dahl-Jensen, D., Hirabayashi, M., Goto-Azuma, K., Hvidberg, C., Kjaer, H., and Satow, K.: Greenland 2012 melt event effects on CryoSat-2 radar altimetry, *Geophys. Res. Lett.*, 42, 3919–3926, <https://doi.org/10.1002/2015GL063296>, 2015.
- Nilsson, J., Gardner, A., Sandberg Sørensen, L., and Forsberg, R.: Improved retrieval of land ice topography from CryoSat-2 data and its impact for volume-change estimation of the Greenland Ice Sheet, *The Cryosphere*, 10, 2953–2969, <https://doi.org/10.5194/tc-10-2953-2016>, 2016.
- Paolo, F., Fricker, H., and Padman, L.: Constructing improved decadal records of Antarctic ice shelf height change from multiple satellite radar altimeters, *Remote Sens. Environ.*, 177, 192–205, <https://doi.org/10.1016/j.rse.2016.01.026>, 2016.
- Pritchard, H., Arthern, R., Vaughan, D., and Edwards, L.: Extensive dynamic thinning on the margins of the Greenland and Antarctic ice sheets, *Nature*, 461, 971–975, <https://doi.org/10.1038/nature08471>, 2009.
- Rémy, F. and Parouty, S.: Antarctic Ice Sheet and Radar Altimetry: A Review, *Remote Sensing*, 1, 1212–1239, <https://doi.org/10.3390/rs1041212>, 2009.
- Richter, A., Popov, S., Dietrich, R., Lukin, V., Fritsche, M., Lipenkov, V., Matveev, A., Wendt, J., Yuskevich, A., and Masolov, V.: Observational evidence on the stability of the hydroglaciological regime of subglacial Lake Vostok, *Geophys. Res. Lett.*, 35, L11502, <https://doi.org/10.1029/2008GL033397>, 2008.
- Richter, A., Popov, S., Fritsche, M., Lukin, V., Matveev, A., Ekyakin, A., Lipenkov, V., Fedorov, D., Eberlein, L., Schröder, L., Ewert, H., Horwath, M., and Dietrich, R.: Height changes over subglacial Lake Vostok, East Antarctica: Insights from GNSS observations, *J. Geophys. Res.-Earth*, 119, 2460–2480, <https://doi.org/10.1002/2014JF003228>, 2014.
- Richter, A., Horwath, M., and Dietrich, R.: Comment on Zwally and others (2015)-Mass gains of the Antarctic ice sheet exceed losses, *J. Glaciol.*, 62, 604–606, <https://doi.org/10.1017/jog.2016.60>, 2016.
- Rignot, E.: Changes in ice dynamics and mass balance of the Antarctic ice sheet, *Philos. T. Roy. Soc. A*, 364, 1637–1655, <https://doi.org/10.1098/rsta.2006.1793>, 2006.
- Rignot, E., Bamber, J., van den Broeke, M., Davis, C., Li, Y., van de Berg, W., and van Meijgaard, E.: Recent Antarctic ice mass loss from radar interferometry and regional climate modelling, *Nat. Geosci.*, 1, 106–110, <https://doi.org/10.1038/ngeo102>, 2008.
- Rignot, E., Mouginot, J., and Scheuchl, B.: Ice Flow of the Antarctic Ice Sheet, *Science*, 333, 1427–1430, <https://doi.org/10.1126/science.1208336>, 2011.
- Rignot, E., Mouginot, J., Morlighem, M., Seroussi, H., and Scheuchl, B.: Widespread, rapid grounding line retreat of Pine Island, Thwaites, Smith, and Kohler glaciers, West Antarctica, from 1992 to 2011, *Geophys. Res. Lett.*, 41, 3502–3509, <https://doi.org/10.1002/2014GL060140>, 2014.
- Rignot, E., Mouginot, J., and Scheuchl, B.: MEaSUREs InSAR-Based Antarctica Ice Velocity Map, Version 2, Boulder, Colorado USA, NASA National Snow and Ice Data Center Distributed Archive, <https://doi.org/10.5067/D7GK8F5J8M8R>, 2017.
- Roemer, S., Legrésy, B., Horwath, M., and Dietrich, R.: Refined analysis of radar altimetry data applied to the region of the subglacial Lake Vostok/Antarctica, *Remote Sens. Environ.*, 106, 269–284, <https://doi.org/10.1016/j.rse.2006.02.026>, 2007.
- Scambos, T. and Shuman, C.: Comment on “Mass gains of the Antarctic ice sheet exceed losses” by H. J. Zwally and others, *J. Glaciol.*, 62, 599–603, <https://doi.org/10.1017/jog.2016.59>, 2016.
- Schröder, L., Richter, A., Fedorov, D., Eberlein, L., Brovkov, E., Popov, S. V., Knöfel, C., Horwath, M., Dietrich, R., Matveev, A. Y., Scheinert, M., Lukin, Valeriy. V. : Kinematic GNSS profiles in central East Antarctica, *PANGAEA*, <https://doi.org/10.1594/PANGAEA.869761>, 2016.
- Schröder, L., Richter, A., Fedorov, D. V., Eberlein, L., Brovkov, E. V., Popov, S. V., Knöfel, C., Horwath, M., Dietrich, R., Matveev, A. Y., Scheinert, M., and Lukin, V. V.: Validation of satellite altimetry by kinematic GNSS in central East Antarctica, *The Cryosphere*, 11, 1111–1130, <https://doi.org/10.5194/tc-11-1111-2017>, 2017.
- Schröder, L., Horwath, M., Dietrich, R., Helm, V., van den Broeke, M. R., Ligtenberg, S. R. M.: Gridded surface elevation changes from multi-mission satellite altimetry 1978–2017, *PANGAEA*, <https://doi.org/10.1594/PANGAEA.897390>, 2019.
- Scott, R., Baker, S., Birkett, C., Cudlip, W., Laxon, S., Mantripp, D., Mansley, J., Morley, J., Rapley, C., Ridley, J., Strawbridge, F., and Wingham, D.: A comparison of the performance of the ice and ocean tracking modes of the ERS-1 radar altimeter over non-ocean surfaces, *Geophys. Res. Lett.*, 21, 553–556, <https://doi.org/10.1029/94GL00178>, 1994.
- Shepherd, A., Ivins, E., A. G., Barletta, V., Bentley, M., Bettadpur, S., Briggs, K., Bromwich, D., Forsberg, R., Galin, N., Horwath, M., Jacobs, S., Joughin, I., King, M., Lenaerts, J., Li, J., Ligtenberg, S., Luckman, A., Luthcke, S., McMillan, M., Meister, R., Milne, G., Mouginot, J., Muir, A., Nicolas, J., Paden, J., Payne, A., Pritchard, H., Rignot, E., Rott, H., Sorensen, L., Scambos, T., Scheuchl, B., Schrama, E., Smith, B., Sundal, A., van Angelen, J., van de Berg, W., van den Broeke, M., Vaughan, D., Velicogna, I., Wahr, J., Whitehouse, P., Wingham, D., Yi, D., Young, D., and Zwally, H.: A Reconciled Estimate of Ice-Sheet Mass Balance, *Science*, 338, 1183–1189, <https://doi.org/10.1126/science.1228102>, 2012.
- Shepherd, A., Ivins, E., Rignot, E., Smith, B., van den Broeke, M., Velicogna, I., Whitehouse, P., Briggs, K., Joughin, I., Krinner, G., Nowicki, S., Payne, T., Scambos, T., Schlegel, N., A. G., Agosta, C., Ahlström, A., Babonis, G., Barletta, V., Blazquez, A., Bonin, J., Csatho, B., Cullather, R., Felikson, D., Fettweis, X., Forsberg, R., Galée, H., Gardner, A., Gilbert, L., Groh, A., Gunter, B., Hanna, E., Harig, C., Helm, V., Horvath, A., Horwath, M., Khan, S., Kjeldsen, K., Konrad, H., Langen, P., Lecavalier, B., Loomis, B., Luthcke, S., McMillan, M., Melini, D., Mernild, S., Mohajerani, Y., Moore, P., Mouginot, J., Moyano, G., Muir, A., Nagler, T., Nield, G., Nilsson, J., Noel, B., Otosaka, I., Pattle, M., Peltier, W., Pie, N., Rietbroek, R., Rott, H., Sandberg-Sørensen, L., Sasgen, I., Save, H., Scheuchl, B., Schrama, E., Schröder, L., Seo, K.-W., Simonsen, S., Slater, T., Spada, G., Sutterley, T., Talpe, M., Tarasov, L., van de Berg, W., van der Wal, W., van Wessem, M., Vishwakarma, B., Wiese, D., and Wouters, B.: Mass balance

- of the Antarctic Ice Sheet from 1992 to 2017, *Nature*, 558, 219–222, <https://doi.org/10.1038/s41586-018-0179-y>, 2018.
- Simonsen, S. and Sørensen, L.: Implications of changing scattering properties on Greenland ice sheet volume change from Cryosat-2 altimetry, *Remote Sens. Environ.*, 190, 207–216, <https://doi.org/10.1016/j.rse.2016.12.012>, 2017.
- Studinger, M.: IceBridge ATM L4 Surface Elevation Rate of Change, Version 1. Updated 2017, Boulder, Colorado USA. NASA National Snow and Ice Data Center Distributed Active Archive Center, <https://doi.org/10.5067/BCW6CI3TXOCY>, 2014.
- Thomas, E., Hosking, J., Tuckwell, R., Warren, R., and Ludlow, E.: Twentieth century increase in snowfall in coastal West Antarctica, *Geophys. Res. Lett.*, 42, 9387–9393, <https://doi.org/10.1002/2015GL065750>, 2015.
- Thomas, R., Davis, C., Frederick, E., Krabill, W., Li, Y., Manizade, S., and Martin, C.: A comparison of Greenland ice-sheet volume changes derived from altimetry measurements, *J. Glaciol.*, 54, 203–212, <https://doi.org/10.3189/002214308784886225>, 2008.
- van Wessem, J. M., van de Berg, W. J., Noël, B. P. Y., van Meijgaard, E., Amory, C., Birnbaum, G., Jakobs, C. L., Krüger, K., Lenaerts, J. T. M., Lhermitte, S., Ligtenberg, S. R. M., Medley, B., Reijmer, C. H., van Tricht, K., Trusel, L. D., van Ulft, L. H., Wouters, B., Wuite, J., and van den Broeke, M. R.: Modelling the climate and surface mass balance of polar ice sheets using RACMO2 – Part 2: Antarctica (1979–2016), *The Cryosphere*, 12, 1479–1498, <https://doi.org/10.5194/tc-12-1479-2018>, 2018.
- Velicogna, I., Sutterley, T., and van den Broeke, M.: Regional acceleration in ice mass loss from Greenland and Antarctica using GRACE time-variable gravity data, *Geophys. Res. Lett.*, 41, 8130–8137, <https://doi.org/10.1002/2014GL061052>, 2014.
- Wingham, D., Rapley, C., and Griffiths, H.: New techniques in satellite altimeter tracking systems, in: *ESA Proceedings of the 1986 International Geoscience and Remote Sensing Symposium (IGARSS'86) on Remote Sensing: Today's Solutions for Tomorrow's Information Needs*, Zürich, Switzerland, 8–11 September 1986, vol. 3, 1339–1344, 1986.
- Wingham, D., Ridout, A., Scharroo, R., Arthern, R., and Shum, C.: Antarctic Elevation Change from 1992 to 1996, *Science*, 282, 456–458, <https://doi.org/10.1126/science.282.5388.456>, 1998.
- Wingham, D., Francis, C., Baker, S., Bouzinac, C., Brockley, D., Cullen, R., Chateau-Thierry, P. d., Laxon, S., Mallow, U., Mavrocordatos, C., Phalippou, L., Ratier, G., Rey, L., Rostan, F., Vieu, P., and Wallis, D.: CryoSat: A mission to determine the fluctuations in Earth's land and marine ice fields, *Adv. Space Res.*, 37, 841–871, <https://doi.org/10.1016/j.asr.2005.07.027>, 2006a.
- Wingham, D., Shepherd, A., Muir, A., and Marshall, G.: Mass balance of the Antarctic ice sheet, *Philos. T. Roy. Soc. A*, 364, 1627–1635, <https://doi.org/10.1098/rsta.2006.1792>, 2006b.
- Wouters, B., Bamber, J., van den Broeke, M., Lenaerts, J., and Sasgen, I.: Limits in detecting acceleration of ice sheet mass loss due to climate variability, *Nat. Geosci.*, 6, 613–616, <https://doi.org/10.1038/ngeo1874>, 2013.
- Wouters, B., Martín-Español, A., Helm, V., Flament, T., van Wessem, J., Ligtenberg, S., van den Broeke, M., and Bamber, J.: Dynamic thinning of glaciers on the Southern Antarctic Peninsula, *Science*, 348, 899–903, <https://doi.org/10.1126/science.aaa5727>, 2015.
- Zwally, H., Giovannetto, M., Li, J., Cornejo, H., Beckley, M., Brenner, A., Saba, J., and Yi, D.: Mass changes of the Greenland and Antarctic ice sheets and shelves and contributions to sea-level rise: 1992–2002, *J. Glaciol.*, 51, 509–527, <https://doi.org/10.3189/172756505781829007>, 2005.
- Zwally, H., Li, J., Robbins, J., Saba, J., Yi, D., and Brenner, A.: Mass gains of the Antarctic ice sheet exceed losses, *J. Glaciol.*, 61, 1019–1036, <https://doi.org/10.3189/2015JoG15J071>, 2015.

Supplement of The Cryosphere, 13, 427–449, 2019  
<https://doi.org/10.5194/tc-13-427-2019-supplement>  
© Author(s) 2019. This work is distributed under  
the Creative Commons Attribution 4.0 License.



*Supplement of*

## **Four decades of Antarctic surface elevation changes from multi-mission satellite altimetry**

**Ludwig Schröder et al.**

*Correspondence to:* Ludwig Schröder ([ludwig.schroeder@tu-dresden.de](mailto:ludwig.schroeder@tu-dresden.de))

The copyright of individual parts of the supplement might differ from the CC BY 4.0 License.

# S1 Data

Table S1: Temporal coverage of the different missions altimetry data.

Mission	From	To
Seasat	1978-07-06	1978-10-10
Geosat	1985-04-01	1989-09-26
ERS-1	1991-08-03*	1996-06-02
ERS-2	1995-05-14	2003-07-02
Envisat	2002-05-14	2012-04-08
ICESat	2003-02-20	2009-10-11
CryoSat-2	2010-07-16	2017-12-31

\* ERS-1 data before 1992-04-14 has not been used, see A.2.

## S1.1 Seasat/Geosat

The observation data of Seasat and Geosat were obtained from the Radar Ice Altimetry project at Goddard Space Flight Center (GSFC, <https://icesat4.gsfc.nasa.gov/index.php>). We used the Ice Data Record (IDR) and for waveform retracking the corresponding Waveform Data Record (WDR). Orbit corrections for JGM-3 orbits were applied and measurements excluded if the noise level of the waveform was too high (flagged in WDR).

In order to make the GSFC data comparable to our reprocessed data in the crossover analysis (Sect. 2.3) we furthermore used the flags indicating that the GSFC-retracking was not successful (leading edge definition failed or problems occurred during retracking). These retracking flags, however, do not apply to our reprocessed data, used in all following processing.

## S1.2 ERS-1/2

For ERS-1 and ERS-2 the SGRD data from the ESA REAPER (Reprocessing altimeter products for ERS) project (Brockley et al., 2017) was used. We excluded measurements where the flags in the data indicated a poor orbital or range measurement quality, where the tracking was lost, where waveforms are corrupted (e.g. due to high noise) and where time jumps in the data occurred as reported by the pre-release calibration/validation ("RA L2 Validation Report", <https://earth.esa.int/documents/10174/1511090/REA-TR-VAL-L2-7001-3-1.pdf>).

Our accuracy and precision tests using crossover (see Sect. 2.2) showed, that the early mission phases of ERS-1, prior to 1992-04-14, contain many outliers which could not be identified by any flag or suspicious value. Thus, we decided to exclude all data of this period from our analysis.

## S1.3 Envisat

For Envisat we used the SGDR V2.1 data from ESA. Here we used the Ku-band measurements of its altimeter system RA-2 acquired during the entire operational period. To remove potentially corrupted observations from the data, we used the *measurement confidence flags* to find recorded distances out of range and to identify problems in the onboard processing and data handling, in the ultra stable oscillator, the automatic gain control or in the waveform samples. We furthermore used the *fault identifier*, the *tracker range validity flag* and the *ICE1 retracking validity flag* to exclude invalid measurements.

## S1.4 ICESat

For ICESat the Release 634 GLA12 dataset from the National Snow and Ice Data Center (NSIDC) was used. We excluded all data where flags indicate a degraded orbit accuracy (e.g. due to off-nadir

operation or orbit maneuvers). We also removed data where the attitude flag indicates any problem with star trackers, gyro or the laser reference sensor. In order to exclude data affected by forward scattering in clouds or drifting snow (e.g. Siegfried et al., 2011), we reject all returns with a gain value exceeding 200, with a reflectivity below 10%, with a misfit between the received waveform and the Gaussian model exceeding 0.03 V or where more than one waveform was detected (Bamber et al., 2009). As the elevation measurements of all other missions refer to the WGS84 ellipsoid, we applied the WGS84 ellipsoid corrections. Furthermore, we applied the saturation correction (Fricker et al., 2005) and corrected the inter-campaign biases according to Schröder et al. (2017).

### S1.5 CryoSat-2

We used the CryoSat-2 L2I product from ESA in the recent processing version Baseline C. For LRM we excluded all data where the *height error flag* indicates problems in the overall height determination. For SARIn mode, we used the retracking scheme described in Helm et al. (2014) using a 40%-TFMRA retracker. The Star Tracker mispointing angles, corrected for the aberration of light, were applied prior the phase processing. This correction is explained in Scagliola et al. (2017) and the data set provided by ESA. "Bad waveforms" are screened using a waveform filter (Helm et al., 2014).

## S2 Reprocessing of radar altimetry

To form a consistent data base, the conventional pulse limited radar altimeter (PLRA) data from the different missions has been reprocessed using a common retracking technique and relocation method. We use the OCOG retracker (Wingham et al., 1986) and the refined relocation method by Roemer et al. (2007) as described in Sect. 2.2. To exclude data from corrupted waveforms in our reprocessed data, we calculated a signal-to-noise ratio (SNR) between the OCOG amplitude and the noise level. We excluded all shots where the SNR is smaller than 3.

In order to assess the precision of the data we calculate near time ( $\Delta t < 31d$ ) ascending-descending crossover differences. As a reference we use the widely applied data processing version of each data center with functional fit retracker (GSFC Version 4  $\beta$ -retracker for Seasat and Geosat, the ICE-2 retracker for ERS and Envisat and the default CFI retracker for CryoSat-2) and the respective slope correction (direct slope correction for GSFC, relocated by mean surface slope for ESA). We compare these standard products with our reprocessed data at 3 different retracking thresholds levels (10%, 20% and 50%). Figure S1 contains the results, binned against surface slope (as in Fig. 2).

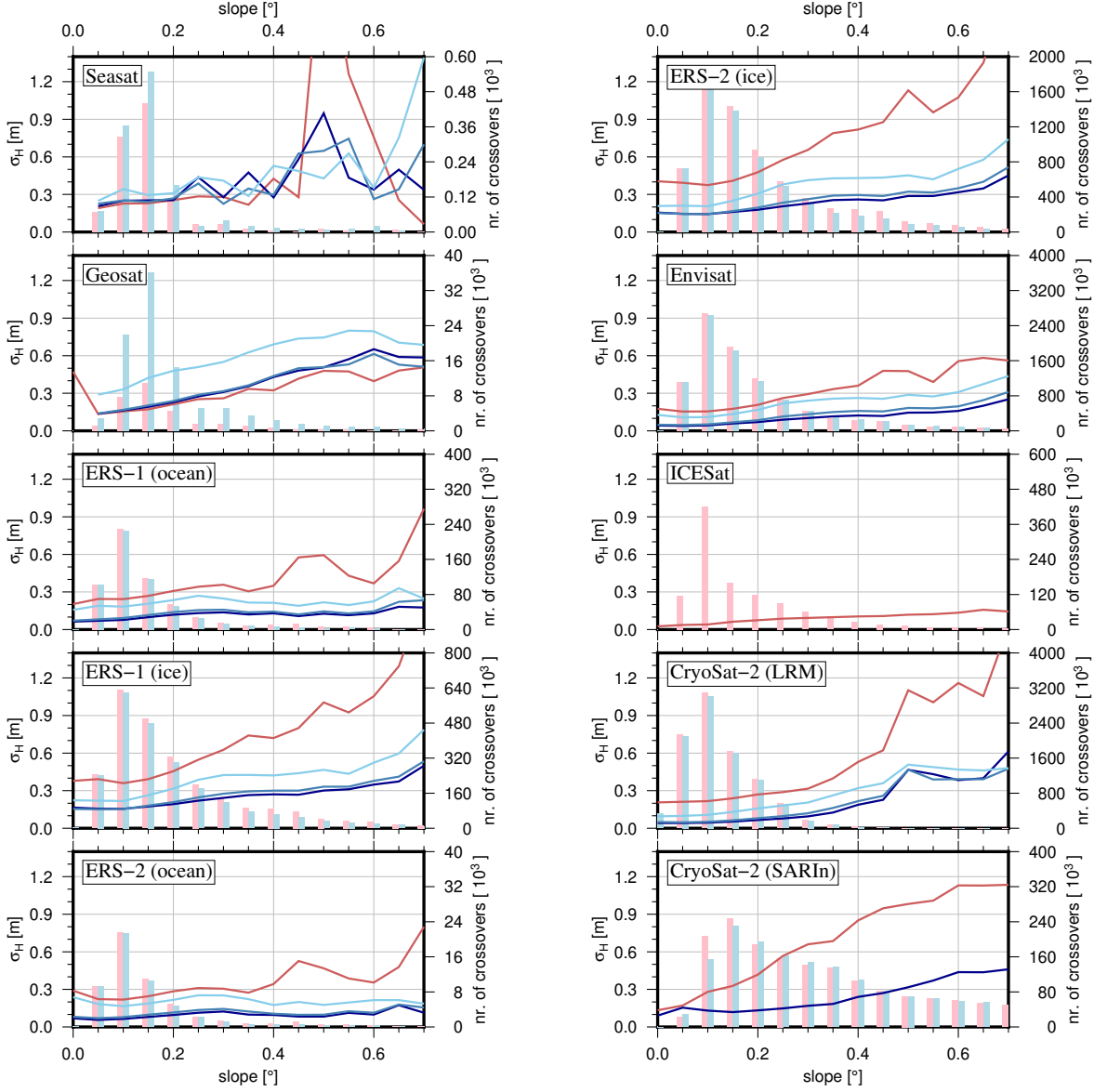


Figure S1: Precision of different processing versions of altimeter measurements from near time ( $<31$  days) crossovers, binned against slope. Red curve: functional fit data provided by the respective data centers (see description above). Light, medium and dark blue curves: Data reprocessed in this study with 50%--, 20%- and 10%-threshold retracker, respectively, relocated using the refined method. For CryoSat-2 SARIn, dark blue stands for 40%-TFMRA retracked data (Helm et al., 2014). Vertical bars: number of crossovers for the standard product (red) and our 10% threshold retracked data (blue).

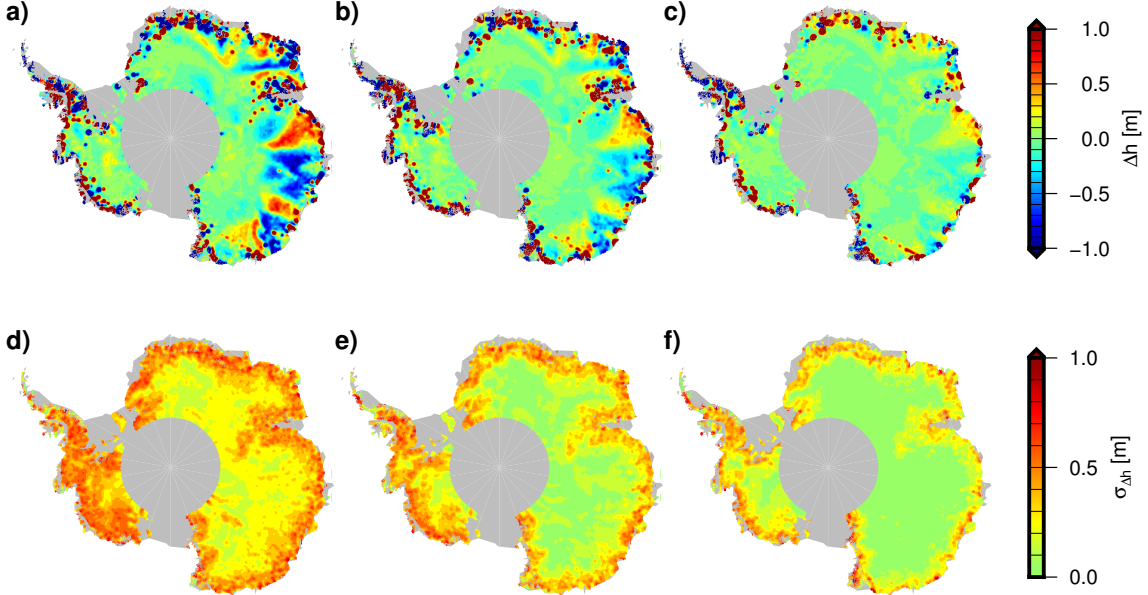


Figure S2: Median offset (**a-c**) and MAD (**d-f**) over  $10 \times 10$  km from short term ( $\Delta t < 31d$ ) crossover differences between ascending and descending orbits for 3 different processing versions of the Envisat data: **a/d**) ESA version with ICE-2 retracker, **b/e**) ESA version with ICE-1 retracker and **c/f**) our reprocessed data with 10%-threshold retracker.

A spatial pattern of the ascending-descending crossover differences (A-D bias) has been noted by Legrésy et al. (1999) and Arthern et al. (2001). However, as shown by Helm et al. (2014), this bias is strongly dependent on the choice of the retracker. Comparing the near time A-D crossover differences of the ESA product of Envisat using the ICE-2 retracker, the ICE-1 retracker (threshold level 30%) and our reprocessed 10% threshold OCOG retracker (Fig. S2) shows that the A-D bias has been significantly reduced. While the ICE-2 data show a well pronounced pattern in the coastal regions with magnitudes of up to a meter, the biases in our product are significantly smaller. In coastal Princess Elizabeth Land (70–90°E), the maximum magnitude still reach 30 cm, while elsewhere, the biases do not exceed 15 cm. The corresponding median absolute deviations (MAD) in the map below show, that these biases are below the remaining noise level.

## S3 Processing of multi-mission SEC time series

### S3.1 Single-mission time series

The single-mission time series are regained from the parameters and monthly averages of the residuals as described in Sect. 3.2. These residuals contain the noise of the measurements and modeling errors (as e.g. nonlinear surface elevation changes or a more complex topography). The monthly average  $\bar{r}_{\text{res}}$  represents the time-dependent modeling errors, i.e. the seasonal and interannual signal, while the remaining modeling errors (i.e., of the topography fit and the backscatter correction) and the noise is subsumed under the standard deviation  $\sigma_{\bar{r}_{\text{res}}}$  of the monthly average. Therefore, we use  $\sigma_{\bar{r}_{\text{res}}}$  as uncertainty estimate for our time series. If this value is larger than 10 m or if it cannot be computed as only one observation is available for this month, we exclude this epoch from the time series.

Figure S3 shows the median of the monthly uncertainty estimates for each data set (before additional uncertainties are added due to corrections in the following steps). In the coastal regions, the observations of Seasat are very sparse, while Geosat data has a high uncertainty. Nevertheless, on the plateau, the noise of the Seasat and Geosat observations is only slightly higher than for the ice mode of ERS. Here, the advantages of both observation modes of ERS become evident. The

ocean mode provides less noise on the plateau while the ice mode data have a much better coverage in the margins. The high noise of CryoSat-2 SARIn near the coast can be explained by its high resolution. This demonstrates that a planar surface of 2 km (which is a compromise between the conditions provided by the different missions and modes involved) cannot adequately represent the detailed topography, sampled by the SARIn data there.

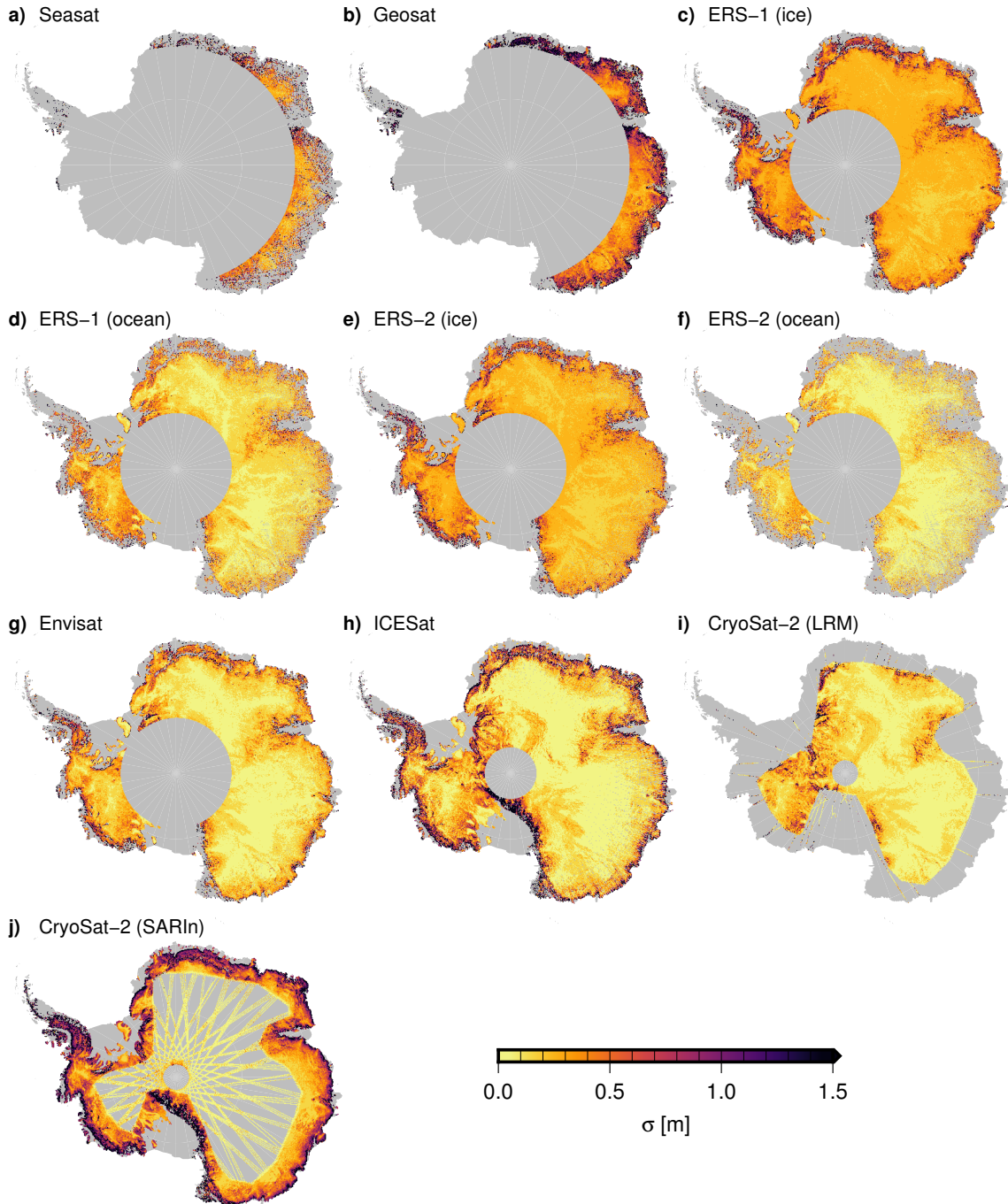


Figure S3: Uncertainty estimates of single-mission time series (median over all epochs of each cell).

## S3.2 Merging PLRA time series

As described in Sect. 3.3, the PLRA satellites sample the topography in the same way and, hence, offsets to merge the time series are valid over larger regional scales. If two missions overlap in time, we use the overlapping epochs to obtain the spatial pattern of the calibration offset. Otherwise, offsets can only be determined where we can assume that the surface elevation change is stable over time. As this cannot deliver the full spatial pattern of offsets, we use a robust overall average to calibrate these missions.

After the offsets are determined as described in the following two subsections, the PLRA time series are corrected and combined. The respective uncertainty estimates are added to the time series and if the data sets overlap, they are averaged using weights according to their uncertainties.

### S3.2.1 Offsets from overlapping epochs

For the missions ERS-1, ERS-2, Envisat and CryoSat-2 in low resolution mode (LRM) we use overlapping epochs for calibration. Therefor, we calculate the time series differences at each cell and for each month observed simultaneously and use the temporal median over all overlapping epochs. In order to obtain an uncertainty estimate for these offsets, we use the MAD of the differences at these epochs. As, however, some outliers might exist in these grids, we apply a spatial outlier filter. We calculate a moving spatial median over 100x100 km and remove any offset that deviates more than 30 cm from the filtered grid. We also exclude any value where the spatial median has been calculated from less than 20 values, i.e. where not enough control data existed. To smooth the offsets and fill the gaps between the ground tracks of the overlapping period, we applied a gaussian filter with  $\sigma = 20$  km. This smoothing was also applied to the squared uncertainties in order to get gridded offset uncertainties.

To form a homogeneous time series, all missions have to be corrected towards one selected reference mission. We chose Envisat for this purpose. In the case of ERS-1, which has no overlap with this reference mission, the offsets need to be summed up. Due to the better spatial and temporal coverage of ERS's ice mode, the ocean mode biases have been determined w.r.t. ice mode and added to the specific ice mode offset. For ERS-1 in ocean mode ( $ERS1_O$ ), this is calculated as

$$\Delta h_{ERS1_O-ENVI} = \Delta h_{ERS1_O-ERS1_I} + \Delta h_{ERS1_I-ERS2_I} + \Delta h_{ERS2_I-ENVI} \quad (S1)$$

The squared uncertainties of the individual offsets were added up. Figure S4 shows the offsets, respectively the sums of offsets, which have been applied to the PLRA single-mission time series.

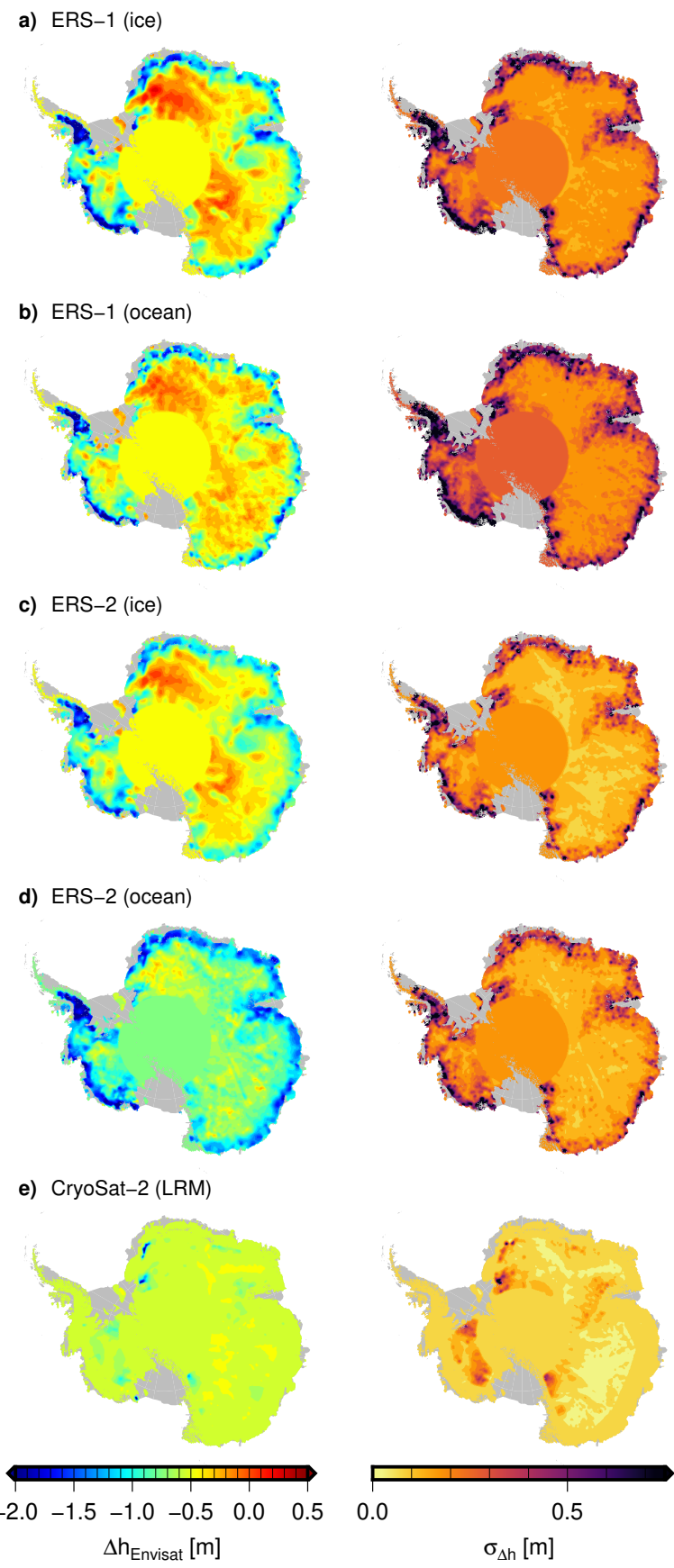


Figure S4: Offsets applied for calibrating the PLRA data with our reference mission Envisat and their uncertainty estimates.

### S3.2.2 Offsets from stable linear trend

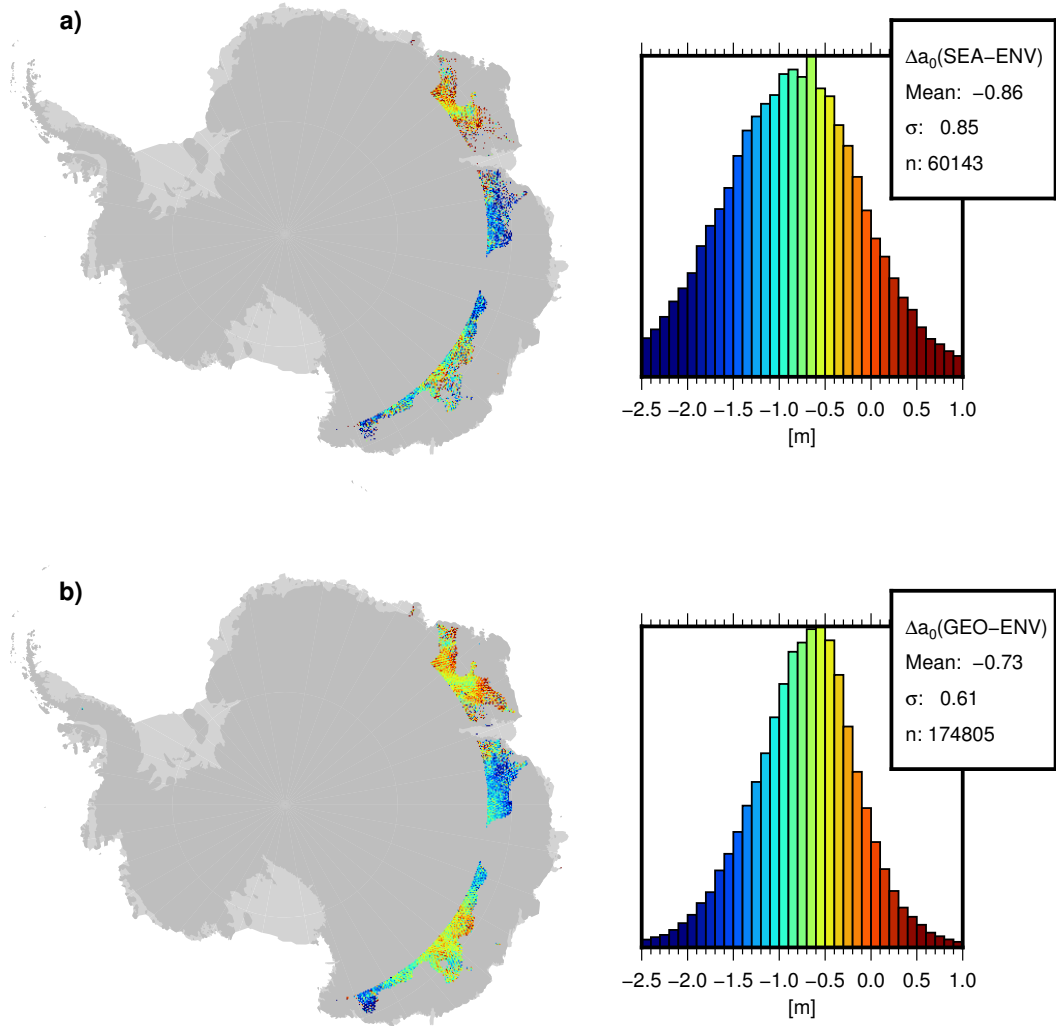


Figure S5: Offsets between **a** Seasat and Envisat and **b** Geosat and Envisat from cells which satisfy our criteria of a stable linear SEC rate.

As described in Sect. 3.3.1, the calibration offsets for Seasat and Geosat are determined from the regions of the AIS, where the a posteriori standard deviation of the trend fit and the FDM indicate a stable linear trend. Figure S5 shows where  $\sigma_{dh/dt} < 1 \text{ cm/yr}$  and  $RMS_{FDM} < 20 \text{ cm}$  are true. The offsets between the respective missions and Envisat reveal that there is a spatial pattern, similar as for later missions. However, these offsets do not represent the whole spatial pattern. Especially in the coastal regions, interannual variations in the elevation changes do not allow the calibration. As it can be seen from the overlapping missions (Fig. S4), a simple extrapolation would not be adequate. Furthermore, our criteria serve as an upper boundary for the variations. Smaller interannual variations may still be present and cannot be separated from the true pattern of offsets. Hence, for the sake of robustness, we decided to apply a mean offset. Here, the influence of remaining interannual variations mitigates significantly over a continental scale. To account for the larger uncertainties, we use the standard deviation of all offsets (0.85 m for Seasat, 0.61 m for Geosat) as the uncertainty of the calibration, which is significantly larger than for the overlapping missions (see uncertainty maps in Fig. S4).

To check the plausibility, we compare these offsets to the values used in other studies. Davis

et al. (1998) report an inter-mission bias of  $27 \pm 4$  cm between Seasat and Geosat from crossover differences over the global oceans. In the notes, they further discuss that other investigations obtained lower sea-surface based biases (e.g.  $22 \pm 4$  cm by G. Kruizinga [thesis, University of Texas, Austin (1997)]). Fricker and Padman (2012) use Seasat in combination with ERS1, ERS-2 and Envisat. They combine these biases of Davis et al. (1998) with other biases for Envisat and finally apply an offset of -0.77 m between Seasat and Envisat.

Within the standard deviation of our estimates, these differences (in the order of magnitude of about a decimeter) are small, but not negligible. However, over ice sheets, the anisotropic surface can have a strong influence on these biases. Legrésy et al. (1999) analyze the A-D biases of ERS-1 and find a clear relationship between the linear polarized measurements and the surface shape. They conclude that merging the circularly polarized altimeter measurements of Seasat and Geosat with linearly polarized measurements of ERS (as well as Envisat) over ice sheets requires extreme care. Thus, we do not rely on the sea-surface based calibration and use the biases determined here.

### S3.3 Merging different techniques

As described in Sect. 3.3.2, offsets of different observation techniques have to be determined for each cell individually due to the different topography sampling. Therefore, we determine an elevation for the reference epoch 09/2010 for each technique and reduce each time series by that reference elevation. To account for uncertainties of the reference elevations, the standard deviations of these fits are combined with the other uncertainty components of the time series by adding the standard uncertainties in square.

Before the final merging step, we remove remaining outliers in the technique specific time series. Especially for the early missions, gross orbit errors offset whole satellite passes. Such systematic outliers cannot be identified by the standard deviation of the residuals. Only after calculating the SEC by removing the reference elevation, they show up clearly against their neighboring passes. Therefore, we utilize a floating median as a robust low-pass filter to identify such outliers. Over a window of 40 km in space and 12 months in time, we calculate the floating median and median absolute deviation (MAD). The MAD indicates the variations on a regional scale and the shorter time scale (i.e. mainly the seasonal signal). To identify probable outliers, we use two thresholds. If the MAD exceeds 50 m, the window is very likely dominated by very noisy data. If, furthermore, the absolute difference  $|SEC_j - \text{Median}(SEC_{\text{window}})|$  exceeds  $0.5 \text{ m} + 3 \cdot MAD_{\text{window}}$ , the data differs significantly from the usual variation in this region and is excluded as well. Near outlet glaciers, where the gradient is large, the  $3 \cdot MAD$  will remove unusual outliers, while in regions with very low variation, the MAD might become very small. Therefore, we add 0.5 m to the outlier criterion to allow for some variation in the data.

The final combination of the techniques is performed using a weighted spatio-temporal averaging with 10 km  $\sigma$  gaussian weights in spatial domain and including the two consecutive epochs in the temporal domain to reduce the noise of a single pass. All filtered time series data within a  $3\sigma$  (30 km) distance in this 3 month window are included but a value is only calculated if at least one data point is closer than 20 km and the central month contains data as well. Hence, the merged multi-mission  $SEC_m$  is calculated from all  $SEC_j$  (for PLRA, SARIn data and laser altimetry) within the given spatio-temporal radius as

$$SEC_m = \frac{\sum W_j \cdot SEC_j}{\sum W_j}. \quad (\text{S2})$$

The weights for each contributing SEC  $j$  are specified according to the respective uncertainty estimate  $\sigma_j$  and the distance to the interpolated location  $d_{j,m}$  as

$$W_j = e^{-\frac{d_{j,m}^2}{(10 \text{ km})^2}} / \sigma_j^2. \quad (\text{S3})$$

We calculate the uncertainty estimate as

$$\sigma_m^2 = \frac{\sum W_j \cdot \epsilon_j^2}{\sum W_j} + \min(\sigma_j)^2. \quad (\text{S4})$$

The first term on the right hand side of this equation is the standard deviation of the contributing  $SEC_j$  from the error propagation, using the residuals of the observations  $\epsilon_j = SEC_j - SEC_m$  and the respective weights. This, however, assumes uncorrelated errors. A systematic error, which influences all measurements within this region, would not be included. Besides the observational noise, our a priori  $\sigma_j$  for each observation include also the systematic errors of the calibration and of the determination of the reference elevation. As a conservative estimate for the systematic effects, we chose the smallest a priori uncertainty in the respective radius and add this value to the standard deviation of the smoothed value.

According to the spatial smoothing implied by our Gaussian weighting function, we reduce our spatial grid resolution to 10x10 km. We did not interpolate a value to cells which are mainly covered by rocks (Burton-Johnson et al., 2016) or outside of the grounded ice sheet (according to the definition of drainage basins).

In the spatial domain, the criterion of a maximum distance of 20 km to any observational data guarantees that a value is only calculated for a 10x10 km cell if we have any data within the radius of a pulse-limited footprint. Grid cells with no valid data within this distance will be left empty and treated as *unobserved*. Similarly, in the temporal domain we calculate grids only if the central month of our 3-month moving average really contains observational data.

## S4 Comparison of SEC with independent data

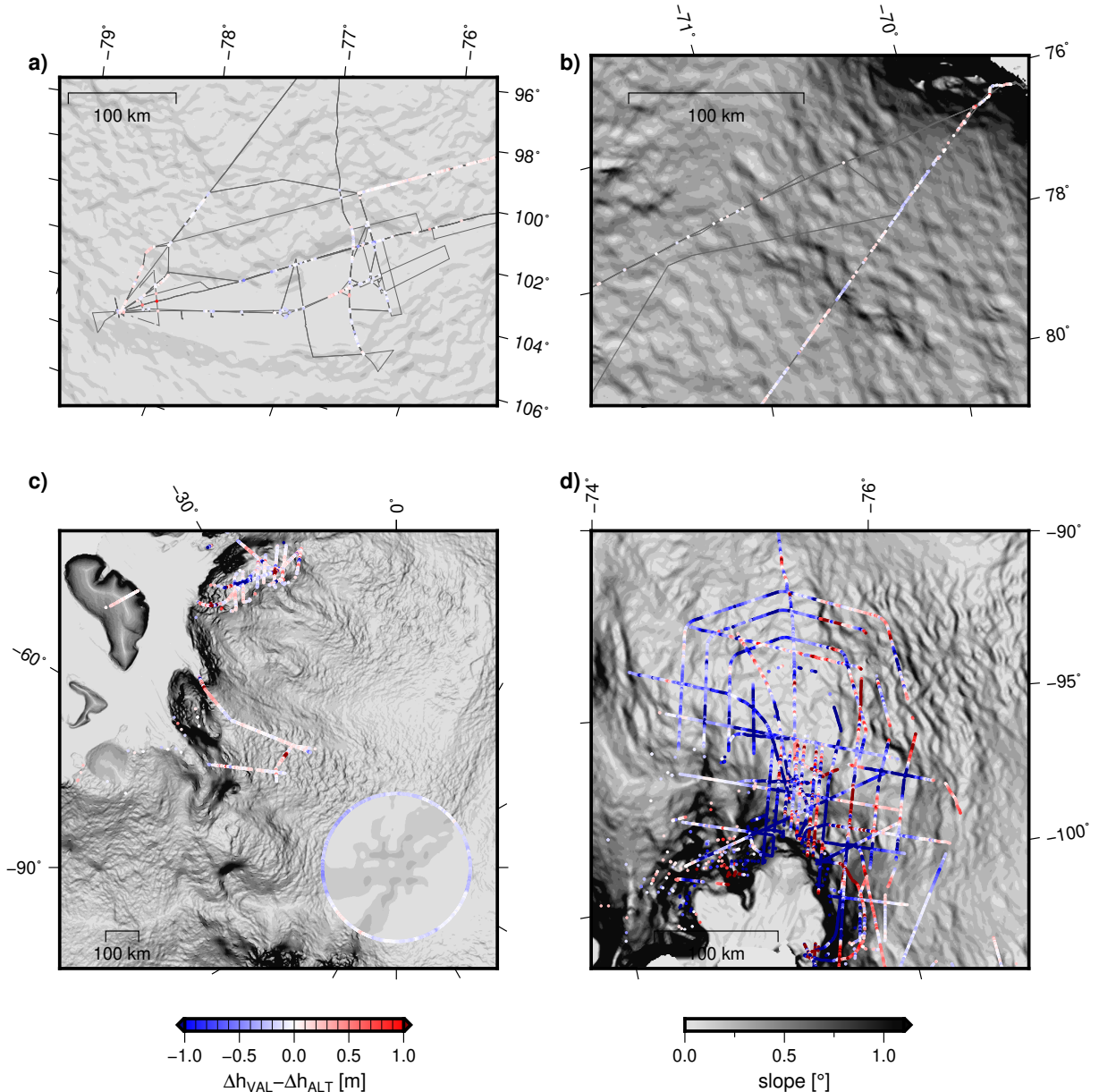


Figure S6: Detailed maps of Fig. 7 a and d of the differences in observed elevation changes between altimetry and validation data for some key regions: Kinematic GNSS - Altimetry at **a)** Lake Vostok and **b)** near Progress Station; Operation IceBridge - Altimetry at **c)** the South Pole and Queen Elizabeth Land and **d)** at Pine Island Glacier.

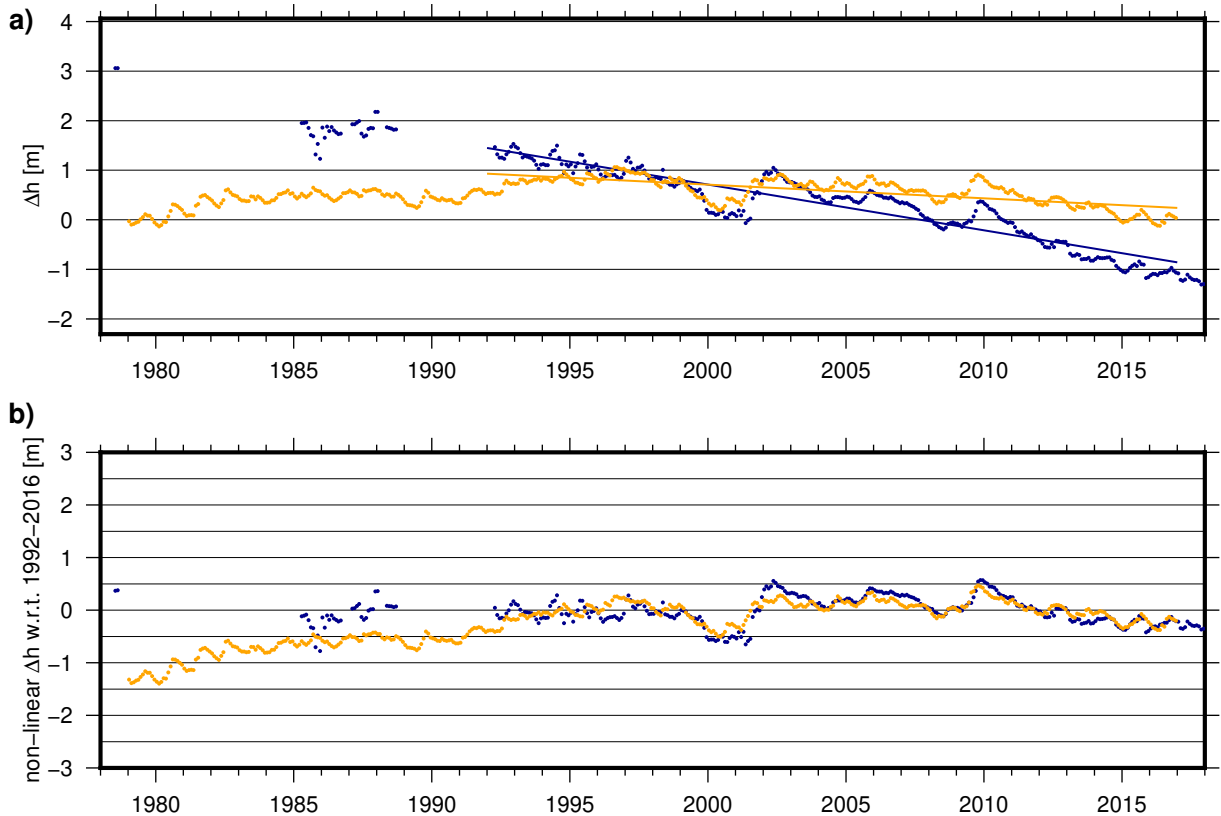


Figure S7: Example for the cross-validation of the altimetry time series (blue) and the FDM (orange). **a)** Total elevation change of both time series for point B at Totten Glacier (cf. Fig. 10b and Tab.2). The solid lines represent the linear trend for 1992–2016 fitted to each time series. **b)** Time series of nonlinear signal component after removing the linear trend from the altimetric SEC and the FDM.

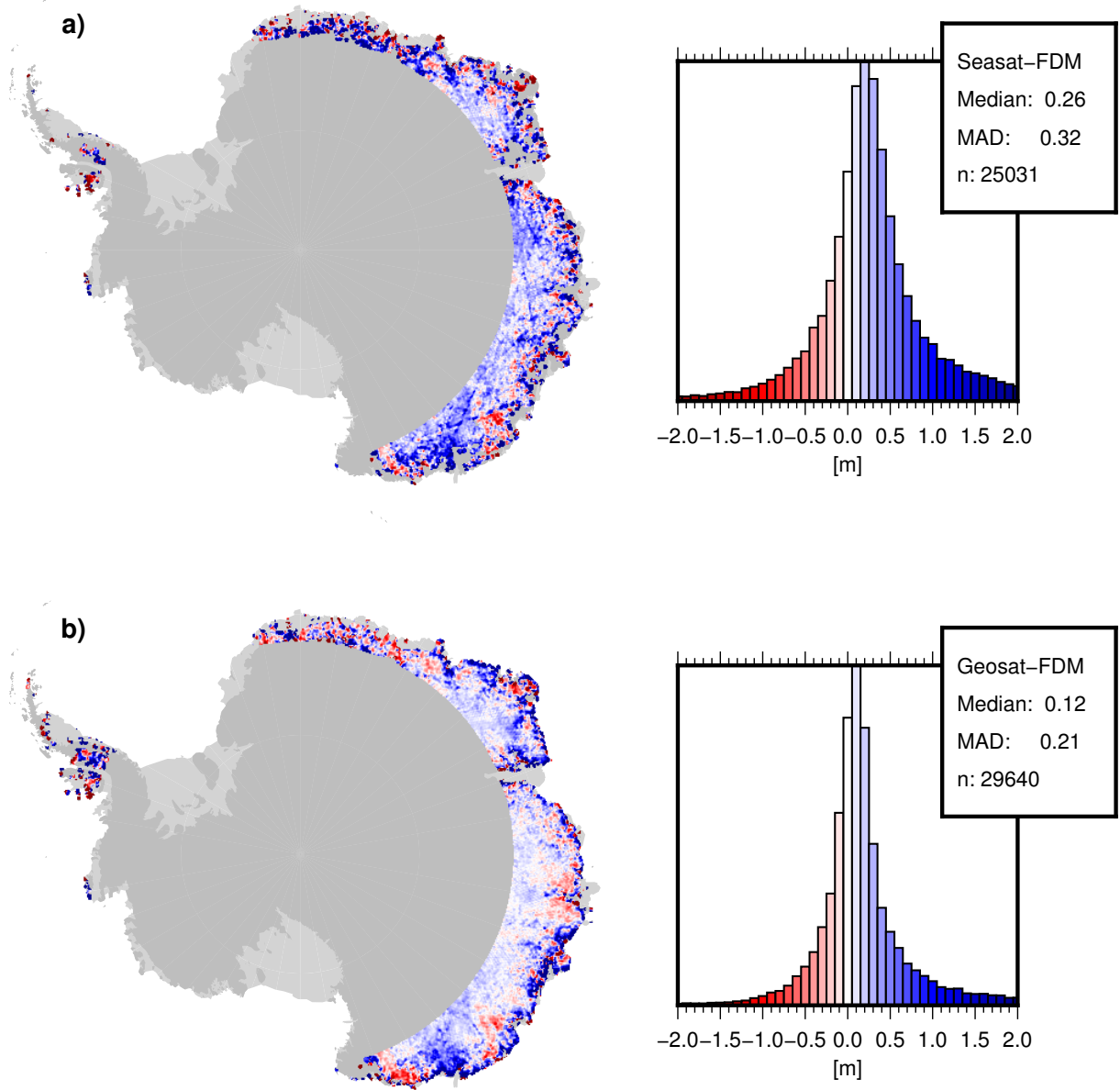


Figure S8: Anomaly differences between **a** Seasat and the FDM and **b** Geosat and the FDM after removing a linear trend, fitted over 1992–2016, from each cell.

## S5 Surface elevation change

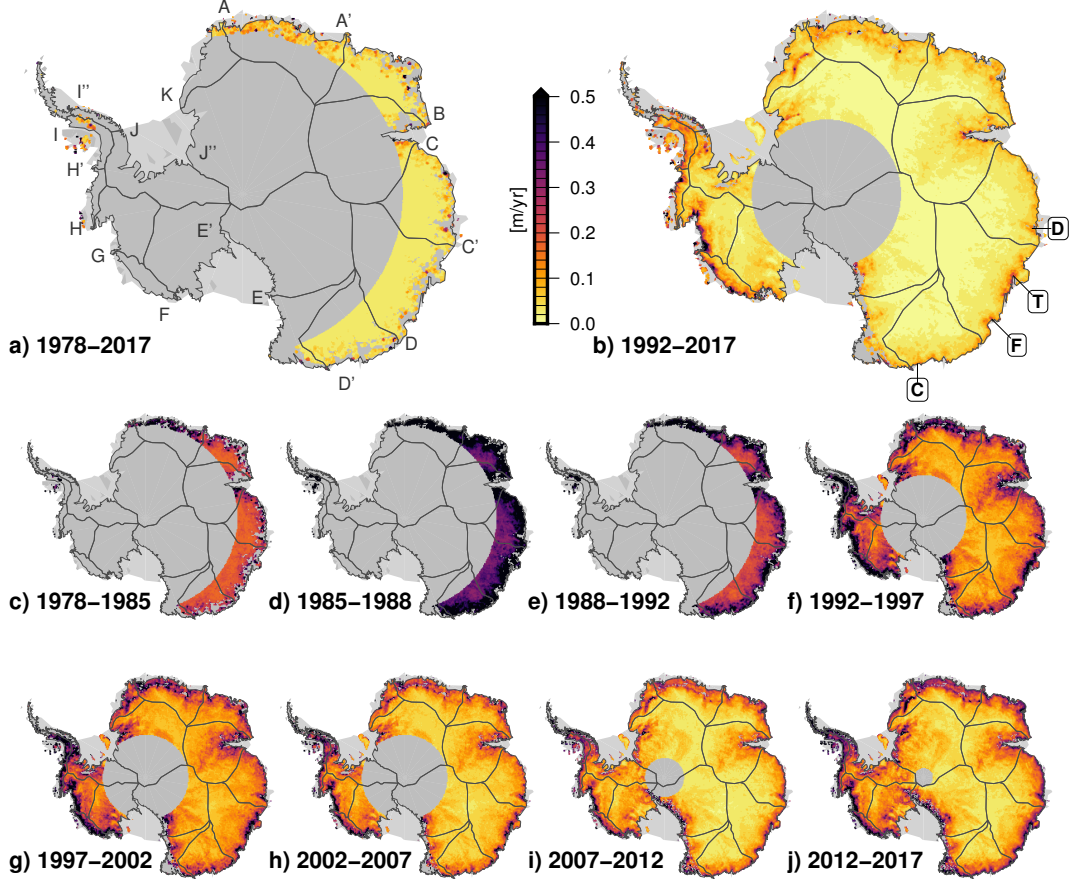


Figure S9: Standard deviation of the multi-mission surface elevation change rates in Fig. 9.

Table S2: Coordinates (polar stereographic, EPSG:3031) and selected results for the points in Fig. 10 (regions: **a** Pine Island Glacier, **b** Totten Glacier, **c** Shirase Glacier and **d** Lake Vostok). The data represent the mean value of the SEC w.r.t 09/2010 over one year. The corresponding uncertainty is the RMS of all uncertainty estimates within this year.

Region	Point	x [m]	y [m]	$SEC_{1978}$	$SEC_{1988}$	$SEC_{1998}$	$SEC_{2008}$	$SEC_{2017}$
<b>a</b>	A	-1590000	-110000	-	-	$9.30 \pm 1.21$	$2.68 \pm 0.40$	$-8.91 \pm 0.94$
<b>a</b>	B	-1590000	-160000	-	-	$13.70 \pm 1.71$	$3.81 \pm 0.55$	$-8.95 \pm 1.25$
<b>a</b>	C	-1580000	-200000	-	-	$20.66 \pm 2.10$	$5.97 \pm 0.74$	$-10.96 \pm 2.22$
<b>a</b>	D	-1580000	-240000	-	-	$30.41 \pm 7.57$	$7.91 \pm 1.88$	$-10.82 \pm 2.74$
<b>b</b>	A	2080000	-790000	$-0.61 \pm 1.07$	$-0.57 \pm 0.75$	$-0.29 \pm 0.74$	$-0.08 \pm 0.18$	$-0.38 \pm 0.52$
<b>b</b>	B	2160000	-890000	$2.91 \pm 1.26$	$1.86 \pm 1.15$	$0.83 \pm 0.69$	$-0.09 \pm 0.25$	$-1.21 \pm 0.66$
<b>b</b>	C	2220000	-960000	$12.18 \pm 3.83$	$8.28 \pm 1.34$	$3.32 \pm 1.48$	$0.33 \pm 0.42$	$-2.83 \pm 1.05$
<b>b</b>	D	2260000	-1000000	-	$14.87 \pm 3.88$	$8.09 \pm 4.54$	$1.92 \pm 1.46$	$-7.60 \pm 4.43$
<b>c</b>	A	1380000	1450000	$-0.02 \pm 1.04$	$-0.11 \pm 0.82$	$-0.22 \pm 0.50$	$-0.30 \pm 0.21$	$0.18 \pm 0.26$
<b>c</b>	B	1380000	1530000	$0.16 \pm 1.11$	$-0.23 \pm 0.90$	$-0.61 \pm 0.62$	$-0.55 \pm 0.26$	$0.23 \pm 0.90$
<b>c</b>	C	1380000	1600000	$0.77 \pm 1.34$	$0.07 \pm 1.54$	$-0.75 \pm 1.18$	$-0.64 \pm 0.39$	$0.11 \pm 0.98$
<b>c</b>	D	1380000	1660000	$0.53 \pm 1.08$	$-0.20 \pm 2.75$	$-2.29 \pm 1.77$	$-0.45 \pm 0.66$	$1.61 \pm 1.52$
<b>d</b>	A	1250000	-360000	-	-	$-0.05 \pm 0.24$	$-0.02 \pm 0.06$	$0.02 \pm 0.08$
<b>d</b>	B	1310000	-370000	-	-	$-0.05 \pm 0.25$	$-0.03 \pm 0.06$	$0.05 \pm 0.08$
<b>d</b>	C	1380000	-370000	-	-	$0.02 \pm 0.26$	$-0.02 \pm 0.07$	$0.04 \pm 0.10$
<b>d</b>	D	1420000	-340000	-	-	$0.07 \pm 0.22$	$-0.02 \pm 0.07$	$0.03 \pm 0.09$

## S6 Ice sheet mass time series

### S6.1 Basins and density

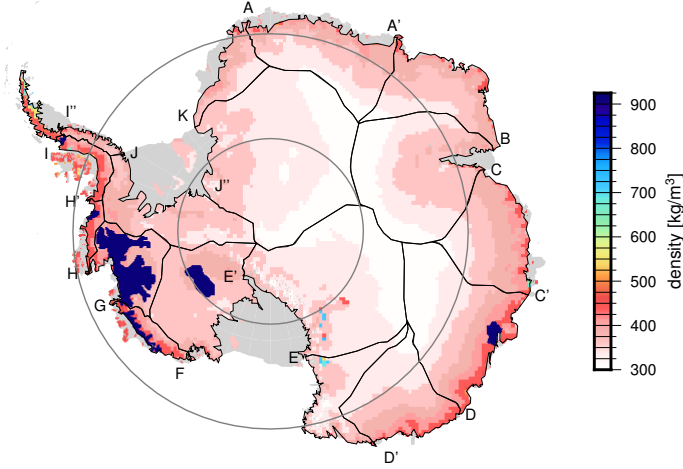


Figure S10: Density mask, adapted after McMillan et al. (2014), with varying firn density from Ligtenberg et al. (2011). The black lines mark the borders of the drainage basins, the gray circles the latitude 72°S and 81.5°S which are the southern limit of several altimetry missions, used.

Table S3: Area [ $10^3 \text{ km}^2$ ] of each basin within the respective zones covered by different missions.

Region	Overall	$< 81.5^\circ\text{S}$	$< 72^\circ\text{S}$
ANT	11892	9391	2913
APIS	232	232	134
EAIS	9620	7764	2779
WAIS	2038	1394	0
A-A'	770	770	233
A'-B	651	651	510
B-C	1310	1310	173
C-C'	707	707	608
C'-D	1161	1161	691
D-D'	696	696	453
D'-E	427	427	93
E-E'	1580	813	0
E'-F	803	450	0
F-G	131	131	0
G-H	419	419	0
H-H'	65	65	0
H'-I	110	110	41
I-I''	61	61	61
I''-J	61	61	31
J-J''	619	327	0
J''-K	2055	966	0
K-A	259	259	15

## S6.2 Uncertainty estimates

In the conversion of the monthly SEC grids into mass anomaly grids, the corrections for GIA  $dh_{GIA}$ , the factor for elastic bedrock response  $\alpha$  and the density mask values  $\rho$  are applied as described in Sect. 5.2. A correction for firn compaction, which would lead to an elevation change without a change in mass, has not been applied here. This effect affects mainly short time scales. Over long time scales, which is the main scope of this paper, only a persistent instability in atmospheric conditions would cause an effect of firn compaction. Such an instability, however, wouldn't be detectable even by firn modeling due to the steady state condition.

The uncertainty estimate for the resulting mass grids are obtained by propagating the formal uncertainties of the contributing data. Here, we denote the uncertainty estimate of the merged SEC grids, obtained from Eq. (S4), by  $\sigma_{SEC}$ . As an estimate for the uncertainty of the density  $\rho$ , we use  $\sigma_\rho = 100 \text{ kg/m}^3$  as in Groh et al. (2014), which accounts for uncertainties due to firn compaction as well. For the GIA correction, we obtain an uncertainty estimate  $\sigma_{GIA}$  from the difference between the models of Ivins et al. (2013) and Whitehouse et al. (2012), propagated to the respective epoch. The uncertainty of the elastic bedrock response factor  $\alpha$  is considered negligible, compared to  $\sigma_{SEC}$ , as it is directly related to the SEC itself. Hence, the gridded values of mass change  $dM$  per area element and the related formal uncertainties  $\sigma_{dM}$  are calculated as

$$\begin{aligned} dM &= \rho \cdot \alpha(dh_{SEC} - dh_{GIA}) \\ \sigma_{dM}^2 &= \rho^2 \cdot \alpha^2(\sigma_{SEC}^2 + \sigma_{GIA}^2) + \alpha^2(dh_{SEC} - dh_{GIA})^2 \cdot \sigma_\rho^2 \end{aligned} \quad (\text{S5})$$

When summing up the mass changes over a basin, however, not all of these uncertainties can be considered uncorrelated. Uncorrelated uncertainties would average out when summed up over many grid cells. However, correlated uncertainties influence all cells in a certain distance in a systematic manner (as e.g. uncertainties in the density over larger regions) and, hence, can lead to much larger uncertainties of the sums. Similar to Wingham et al. (1998), we calculated the autocovariance of the SEC in different regions and found sufficient decorrelation for distances longer than 50 km. This radius corresponds to an area of  $\pi \cdot (50 \text{ km})^2$  or 78.5 grid-cells of  $A=10 \times 10 \text{ km}$ . Therefore, we applied a scaling factor of  $\beta = 78.5$  to the squared uncertainties in order to account for the autocorrelation over the area.

Besides the uncertainty of the observed cells  $o$ , an additional uncertainty in the sums comes from the unobserved cells  $u$ . To account for the changes which could not be observed by altimetry, we used the mass trends from GRACE. They originate from spherical harmonics and, hence, are free of gaps. We calculated a  $dM$  grid for the respective epoch from the linear GRACE trends and summed those  $dM$  up over all cells which are not observed by altimetry within a basin. Summed up over all observed ( $o$ ) and unobserved ( $u$ ) cells of the respective basin, these two components are used to obtain the total uncertainty  $\sigma_\Sigma$  for each epoch as

$$\sigma_\Sigma^2 = \sum_o A \cdot \beta \cdot \sigma_{dM,o}^2 + \sum_u A \cdot dM_u^2, \quad (\text{S6})$$

These uncertainty estimates are displayed in the plots of summed mass time series (Figs. 11, 12 and 13).

## S6.3 Correlation with independent data

A comparison of the mass change rates obtained from altimetry and GRACE in Tab. S4 shows that GRACE observes a significantly larger mass gain of the EAIS (see also Fig. 11). Also for the APIS, there are substantial differences. The correlation coefficients  $r$  have been calculated from the anomalies of both time series. For the total Antarctic time series ( $<81.5^\circ\text{S}$ ), the correlation coefficient between altimetry and GRACE (for the time period 2002-2016) of 0.96 demonstrates that the interannual variability, measured by both types of observations, agrees very well. At the EAIS, the signals are more dominated by remaining issues in the processing of both data sets.

Table S4: Comparison of the mass time series for the AIS ( $<81.5^{\circ}\text{S}$ ) between the altimetry and the two independent datasets over simultaneously observed periods. The mass change rates for the corresponding data and time interval are calculated as in Tab. 2. The correlation coefficients  $r$  refer to the respectively detrended anomalies.

region	2002-2016			1992-2016		
	dM/dt [Gt/yr]		$r_{GRACE}$	dM/dt [Gt/yr]		$r_{SMBA}$
	altimetry	GRACE		altimetry	SMBA	
AIS	-109.9 $\pm$ 15.6	-88.7	0.962	-84.7 $\pm$ 15.5	-2.2	0.604
EAIS	9.6 $\pm$ 6.9	42.1	0.558	4.9 $\pm$ 5.0	-6.2	0.635
WAIS	-119.1 $\pm$ 11.4	-113.7	0.997	-91.7 $\pm$ 10.3	1.3	0.838
APIS	-0.4 $\pm$ 7.2	-17.1	0.901	2.1 $\pm$ 8.9	2.7	0.535

A similar comparison has been performed with the SMBA over the time period 1992-2017. With coefficients between 0.60 and 0.84, this correlation is lower, compared to GRACE, but still, the agreement is remarkable.

## References

- Arthern, R., Wingham, D., and Ridout, A.: Controls on ERS altimeter measurements over ice sheets: Footprint-scale topography, backscatter fluctuations, and the dependence of microwave penetration depth on satellite orientation, *Journal of Geophysical Research – Atmospheres*, 106, 33 471–33 484, <https://doi.org/10.1029/2001JD000498>, 2001.
- Bamber, J., Gomez-Dans, J., and Griggs, J.: A new 1 km digital elevation model of the Antarctic derived from combined satellite radar and laser data – Part 1: Data and methods, *The Cryosphere*, 3, 101–111, <https://doi.org/10.5194/tc-3-101-2009>, 2009.
- Brockley, D., Baker, S., Femenias, P., Martinez, B., Massmann, F.-H., Otten, M., Paul, F., Picard, B., Prandi, P., Roca, M., Rudenko, S., Scharroo, R., and Visser, P.: REAPER: Reprocessing 12 Years of ERS-1 and ERS-2 Altimeters and Microwave Radiometer Data, *IEEE Trans. Geosci. Remote Sens.*, 55, 5506–5514, <https://doi.org/10.1109/TGRS.2017.2709343>, 2017.
- Burton-Johnson, A., Black, M., Fretwell, P., and Kaluza-Gilbert, J.: An automated methodology for differentiating rock from snow, clouds and sea in Antarctica from Landsat 8 imagery: a new rock outcrop map and area estimation for the entire Antarctic continent, *The Cryosphere*, 10, 1665–1677, <https://doi.org/10.5194/tc-10-1665-2016>, 2016.
- Davis, C., Kluever, C., and Haines, B.: Elevation Change of the Southern Greenland Ice Sheet, *Science*, 279, 2086–2088, <https://doi.org/10.1126/science.279.5359.2086>, 1998.
- Fricker, H. and Padman, L.: Thirty years of elevation change on Antarctic Peninsula ice shelves from multimission satellite radar altimetry, *J. Geophys. Res.*, 117, <https://doi.org/10.1029/2011JC007126>, 2012.
- Fricker, H., Borsa, A., Minster, B., Carabajal, C., Quinn, K., and Bills, B.: Assessment of ICESat performance at the salar de Uyuni, Bolivia, *Geophys. Res. Lett.*, 32, L21S06, <https://doi.org/10.1029/2005GL023423>, 2005.
- Groh, A., Ewert, H., Rosenau, R., Fagiolini, E., Gruber, C., Floricioiu, D., Abdel Jaber, W., Linow, S., Flechtner, F., Eineder, M., Dierking, W., and Dietrich, R.: Mass, volume and velocity of the Antarctic Ice Sheet: present-day changes and error effects, *Surv. Geophys.*, 35, 1481–1505, <https://doi.org/10.1007/s10712-014-9286-y>, 2014.
- Helm, V., Humbert, A., and Miller, H.: Elevation and elevation change of Greenland and Antarctica derived from CryoSat-2, *The Cryosphere*, 8, 1539–1559, <https://doi.org/10.5194/tc-8-1539-2014>, 2014.
- Ivins, E., James, T., Wahr, J., Schrama, E., Landerer, F., and Simon, K.: Antarctic contribution to sea level rise observed by GRACE with improved GIA correction, *J. Geophys. Res. Solid Earth*, 118, 3126–3141, <https://doi.org/10.1002/jgrb.50208>, 2013.
- LeGrésy, B., Rémy, F., and Schaeffer, P.: Different ERS altimeter measurements between ascending and descending tracks caused by wind induced features over ice sheets, *Geophys. Res. Lett.*, 26, 2231–2234, <https://doi.org/10.1029/1999GL900531>, 1999.
- Ligtenberg, S., Helsen, M., and van den Broeke, M.: An improved semi-empirical model for the densification of Antarctic firn, *The Cryosphere*, 5, 809–819, <https://doi.org/10.5194/tc-5-809-2011>, 2011.
- McMillan, M., Shepherd, A., Sundal, A., Briggs, K., Muir, A., Ridout, A., Hogg, A., and Wingham, D.: Increased ice losses from Antarctica detected by CryoSat-2, *Geophys. Res. Lett.*, 41, 3899–3905, <https://doi.org/10.1002/2014GL060111>, 2014.
- Roemer, S., LeGrésy, B., Horwath, M., and Dietrich, R.: Refined analysis of radar altimetry data applied to the region of the subglacial Lake Vostok / Antarctica, *Remote Sens. Environ.*, 106, 269–284, <https://doi.org/10.1016/j.rse.2006.02.026>, 2007.
- Scagliola, M., Fornari, M., Bouffard, J., and Parrinello, T.: The CryoSat interferometer: End-to-end calibration and achievable performance, *Adv. Space Res.*, <https://doi.org/10.1016/j.asr.2017.09.024>, 2017.

- Schröder, L., Richter, A., Fedorov, D., Eberlein, L., Brovkov, E., Popov, S., Knöfel, C., Horwath, M., Dietrich, R., Matveev, A., Scheinert, M., and Lukin, V.: Validation of satellite altimetry by kinematic GNSS in central East Antarctica, *The Cryosphere*, 11, 1111–1130, <https://doi.org/10.5194/tc-11-1111-2017>, 2017.
- Siegfried, M., Hawley, R., and Burkhart, J.: High-Resolution Ground-Based GPS Measurements Show Intercampaign Bias in ICESat Elevation Data Near Summit, Greenland, *Geoscience and Remote Sensing, IEEE Transactions on*, 49, 3393–3400, <https://doi.org/10.1109/TGRS.2011.2127483>, 2011.
- Whitehouse, P., Bentley, M., Milne, G., King, M., and Thomas, I.: A new glacial isostatic adjustment model for Antarctica: calibrated and tested using observations of relative sea-level change and present-day uplift rates, *Geophys. J. Int.*, 190, 1464–1482, <https://doi.org/10.1111/j.1365-246X.2012.05557.x>, 2012.
- Wingham, D., Rapley, C., and Griffiths, H.: New techniques in satellite altimeter tracking systems, in: *ESA Proceedings of the 1986 International Geoscience and Remote Sensing Symposium(IGARSS'86) on Remote Sensing: Today's Solutions for Tomorrow's Information Needs*, vol. 3, pp. 1339–1344, Zürich, 1986.
- Wingham, D., Ridout, A., Scharroo, R., Arthern, R., and Shum, C.: Antarctic Elevation Change from 1992 to 1996, *Science*, 282, 456–458, <https://doi.org/10.1126/science.282.5388.456>, 1998.